




# Switching between Z-scheme and type-II charge separation mechanisms in ZnO/ZnS composite photocatalyst by La doping

Fucheng Yu<sup>1,\*</sup> , Yadong Zhou<sup>1</sup>, Junpeng Cui<sup>1</sup>, Zhengyan Liu<sup>1</sup>, Yuanmeng Li<sup>1</sup>, Ling He<sup>1</sup>, Jianbin Zhang<sup>1</sup>, Xianxi Tang<sup>1</sup>, and Yangshuo Liu<sup>2</sup>

<sup>1</sup>School of Material Science and Engineering, Lanzhou University of Technology, Lanzhou 730050, People's Republic of China

<sup>2</sup>Hubei Key Laboratory of Biomass Fibers and Eco-Dyeing and Finishing, Wuhan Textile University, Wuhan 430073, People's Republic of China

Received: 3 August 2021

Accepted: 29 October 2021

Published online:  
3 January 2022

© The Author(s), under exclusive licence to Springer Science+Business Media, LLC, part of Springer Nature 2021

## ABSTRACT

In order to study the photo-generated carrier transfer mechanism in ZnO/ZnS-based composite photocatalyst, a series of ZnO/ZnS composite samples were prepared by two-step method. Firstly, La-doped ZnO nanorods were grown on silica substrates with hydrothermal method, and then the nanorods were sulfurized in situ to form ZnO/ZnS heterojunctions. The effect of La doping concentration on the structural properties of ZnO nanorods was investigated. With the increase in La doping concentration, the diameter and density of ZnO nanorods increase, but when the doping concentration reaches 2.0%, ZnO crystal quality degrades. Therefore, the ZnO nanorods with La doping concentration of 1.5% were used as matrix to study the effect of sulfurization time on the properties of ZnO/ZnS-based composite. With the increase in sulfurization time, the UV-vis absorbance of the samples first increases and then decreases. The composite photocatalyst with sulfurization time of 60 min shows the best UV-vis absorbance, and its photocatalytic performance is also the best. Then, the photo-generated carrier transfer mechanism in the ZnO/ZnS-based composite was studied. Because the Fermi level of ZnS is higher than that of ZnO, the electrons in ZnS would be transferred to ZnO when they form a heterojunction, then a built-in electric field is constructed from ZnS to ZnO. Generally, the photo-generated carrier transfer mechanism in ZnO/ZnS heterojunction follows a Z-scheme mechanism. However, when La element is doped at a concentration of 1.5%, the Fermi level ZnO is increased and higher than that of ZnS. Then, the electrons in ZnO are transferred to ZnS to form a new built-in electric field from ZnO to ZnS in the heterojunction, and its direction is opposite to that of the undoped ZnO/ZnS composite sample. Then, the photo-

Handling Editor: Pedro Camargo.

Address correspondence to E-mail: yufc72@163.com

<https://doi.org/10.1007/s10853-021-06683-7>

generated carrier transfer mechanism in the composite is changed to type-II. Therefore, the photo-generated carrier transfer mechanism in the ZnO/ZnS-based composite can be tailored by La doping concentration.

## Introduction

Photocatalytic degradation technology is one of the effective methods to solve the problem of environmental pollution. Then, the research on photocatalyst materials has become a hot topic for researchers, such as ZnO, TiO<sub>2</sub> and other materials [1–4]. In fact, due to the limitation of light absorption capacity, low photoelectric conversion efficiency, high recombination rate of photo-generated electrons and holes and low carrier mobility, simple semiconductor materials is difficult to be directly applied in photocatalysis. Therefore, it is necessary to prepare composite photocatalysts containing semiconductor components to improve visible light absorption capacity, separate photo-generated electron–hole pairs, or obtain strong redox ability [5], so as to make the application of photocatalytic technology in practice possible. In a composite photocatalyst, whether the carriers can transfer through the component interface depends on the energy band relationship of the components. For example, when two semiconductors with different Fermi levels form a junction, electrons will transfer through the interface from the high Fermi level side to the low Fermi level side until the two Fermi levels are equal [6, 7]. Thus, on both sides of the interface, free electrons are depleted in the semiconductor on the original high Fermi level side and accumulated in the semiconductor on the low Fermi level side, forming a built-in electric field at the interface [8]. Finally, on both sides of the interface, the bands of the high Fermi level semiconductor bend upward, and those of the low Fermi level semiconductor bend downward [9]. As a result, the photo-generated electrons near the interface will transfer in the opposite direction to the built-in electric field. The downward bending bands allow electrons to flow out, but do not allow holes to flow out, while the upward bending bands prohibit electrons from flowing out, but allow holes to flow out. This characteristic of composite photocatalysts plays an important role in driving the opposite transfer of photo-generated electrons and holes, so as to inhibit

the recombination of photo-generated electrons and holes in each component. In p–n heterojunction, the Fermi level change and band bending of semiconductor components are shown in Fig. 1, where “CB” is conduction band, “VB” is valence band, and “E<sub>F</sub>” is Fermi level [10, 11].

There are two possible common types of carrier transfer mechanism in multi-semiconductor composites, namely Z-scheme and type-II, which are determined by the electron transfer path through the interface between components [7]. For Z-type carrier transfer mechanism in semiconductor composites, the electrons in the conduction band (CB) of one semiconductor are transferred to the valence band (VB) of another semiconductor and combined with the holes there, leaving holes in the VB of the former and electrons in the CB of the latter. While for type-II carrier transfer mechanism in composites, electrons in the CB of the high Fermi level semiconductor flow to the CB of the low Fermi level semiconductor, while holes flow in the opposite direction in the composites. Therefore, in composite photocatalysts, photo-generated electrons and holes are separated into two different semiconductor components whether carriers transfer in Z-scheme or type-II mechanism. Generally, for a given composite photocatalyst, the redox potential with type-II carrier transfer mechanism is lower than that with Z-scheme carrier transfer mechanism. However, compared with carrier loss in Z-scheme carrier transfer mechanism, more carriers can participate in photocatalytic reaction in type-II carrier transfer mechanism [12]. Although a well-designed composite photocatalyst generally shows better photocatalytic performance than a single semiconductor photocatalyst, the properties of different components and interfacial barrier directly affect the photocatalytic properties of the composite photocatalyst. Therefore, the selection of composite photocatalyst component materials is very important. ZnO is a wide band gap n-type semiconductor, which has the advantages of high electron mobility, non-toxic and low cost, so it has become a potential component of composite photocatalyst. In addition, ZnS has the same crystal structure and similar

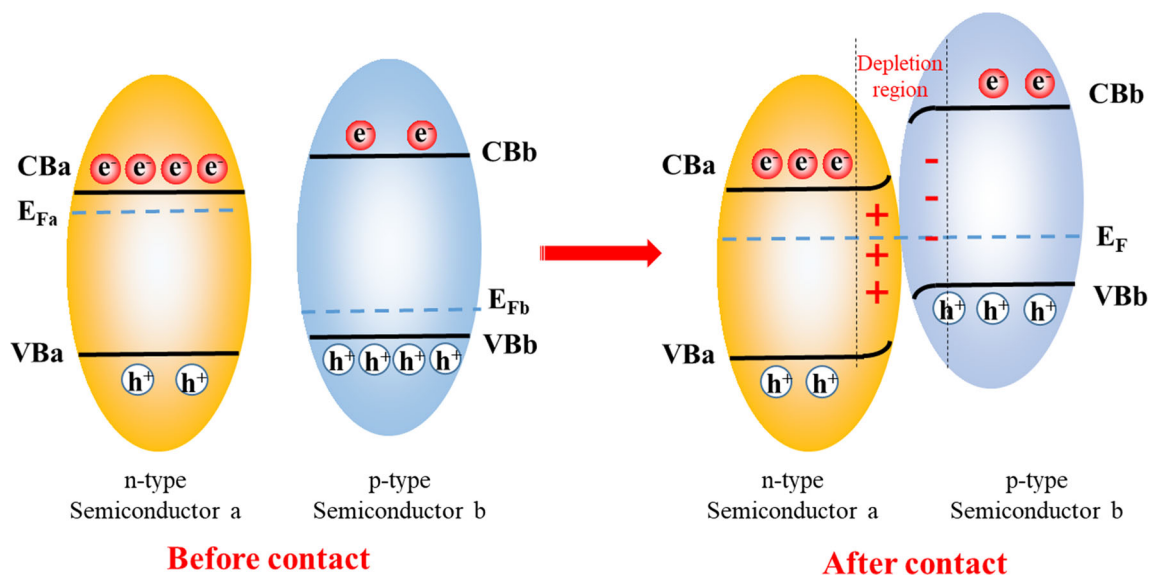


**Figure 1** Schematic diagram of band coupling between semiconductor components when p–n heterojunction is formed.

physical properties as ZnO [13]. After deposited on the surface of ZnO matrix, the interfacial potential barrier can be effectively reduced, and the charge transfer through the interface is easier [5, 14]. Generally, the photo-generated carrier transfer mechanism in ZnO/ZnS heterojunction is Z-scheme [14, 15].

How to adjust the carrier transfer mechanism in a composite photocatalyst? It is a feasible solution to change the carrier transfer way through the interface by adjusting the Fermi levels of the composite components [16]. In this case, the adjustment of Fermi level of semiconductor components has become very meaningful, and many adjustment methods have been reported. Single element donor doping in semiconductor could generally increase the electron concentration in the semiconductor, so as to improve its Fermi level [17–21], while acceptor doping could decrease the Fermi level of the semiconductor [16]. Furthermore, multi-element co-doping showed greater flexibility to adjust semiconductor Fermi level. Donor–acceptor co-doping in semiconductor showed a large adjustable range of Fermi level [22]. After fixing the oxygen vacancy ( $O_V$ ) defects in crystal by multi-element co-doping, the adjustment of Fermi level showed better controllability [23, 24]. In addition, surface treatment of semiconductors could also affect the Fermi level of semiconductors, such as atmosphere treatment [25, 26], interface effect [27, 28] and surface geometry treatment [29].

Without considering redox ability, ZnO/ZnS heterojunction with type-II carrier transfer

mechanism can provide more carriers to participate in photocatalytic reaction than that with Z-scheme carrier transfer mechanism, which is conducive to improve its photocatalytic degradation efficiency. Therefore, it is necessary to study the formation conditions of type-II photo-generated carrier transfer mechanism in ZnO/ZnS-based composites. In this study, ZnO/ZnS composite photocatalyst with Z-scheme carrier transfer mechanism was first prepared, and then the switching possibility of carrier transfer mechanism from Z-scheme to type-II has been studied by controlling La doping concentration in ZnO nanorods.

## Experiments

### Preparation of ZnO/ZnS composite photocatalyst

ZnO nanorods were grown on a silica substrate by hydrothermal method, which is the same as that in our previous studies [30, 31]. ZnO seed layer was first deposited on a silica substrate by sol–gel method, and then La-doped ZnO nanorods were grown on the seed layer by hydrothermal method. In this process, lanthanum nitrate hexahydrate ( $La(NO_3)_3 \cdot 6H_2O$ ) was used as the doping precursor of ZnO nanorods, and the amounts of  $La^{3+}$  in hydrothermal solution were 0.5%, 1.0%, 1.5% and 2.0% of the molar ratio of  $Zn^{2+}$ , respectively. The samples of hydrothermal-

grown ZnO nanorods with a length of about 1.5  $\mu\text{m}$  were labeled as “ZnO- $c$ ” ( $c = 0, 0.5, 1.0, 1.5$  or  $2.0$ ) [31]. Deionized (DI) water of 40 mL was poured into a beaker containing 200 mg of thiourea ( $\text{CH}_4\text{N}_2\text{S}$ ) and ultrasonicated for 5 min, and then a uniform solution was obtained. The solution was transferred to a 100-mL autoclave containing ZnO nanorods sample, and kept at 180 °C for 40 min, 50 min, 60 min or 70 min. The partially sulfurized ZnO nanorod sample was labeled as “ZnS- $T$ ” ( $T = 40, 50, 60$  or  $70$ ). The pure ZnS sample was obtained by the same method but with longer sulfurization time. The sample synthetic process is shown in Fig. 2.

### Characterizations

The structural properties of the samples were characterized by X-ray diffraction (XRD, D8-ADVANCE). The surface morphology of the samples was examined by a cold field emission scanning electron microscope (FESEM, JMS-6700F) and transmission electron microscope (TEM, JEM-2010). The elemental composition of the samples was analyzed by an energy dispersive X-ray spectrometer (EDXS). The optical properties of the samples were studied with an ultraviolet–visible spectrophotometer (PE Lambda 35) and fluorescence spectrophotometer (PL, fluorescence spectrophotometer, F97 pro) with an excitation wavelength of 254 nm. The element binding states of the samples were analyzed by an X-ray photoelectron spectroscopy (XPS, Thermo Scientific<sup>TM</sup>, K-Alpha<sup>TM</sup>, Thermo Fisher). And the electrochemical impedance spectroscopy (EIS) of the

samples was examined by an electrochemical workstation (CHI660D).

### Photocatalytic property test

Under simulated sunlight irradiation (Xe lamp, CEL-S500/350, 300 nm–2500 nm), the photocatalytic properties of the samples were tested by the photocatalytic degradation efficiency of methylene blue (MB) solution with an initial concentration of 30 mg/L. After the sample on substrate was put into a cuvette containing 4 mL of 30 mg/L MB solution, it was kept in the dark for 15 min, and then irradiated with simulated sunlight. The distance between the Xe lamp and the MB solution surface was 15 cm. Under the photocatalytic action of the sample, the intrinsic absorbance of MB solution at 665 nm was checked every 15 min, indicating the concentration change of MB solution. The degradation efficiency ( $\eta$ ) of the sample was calculated as follows:

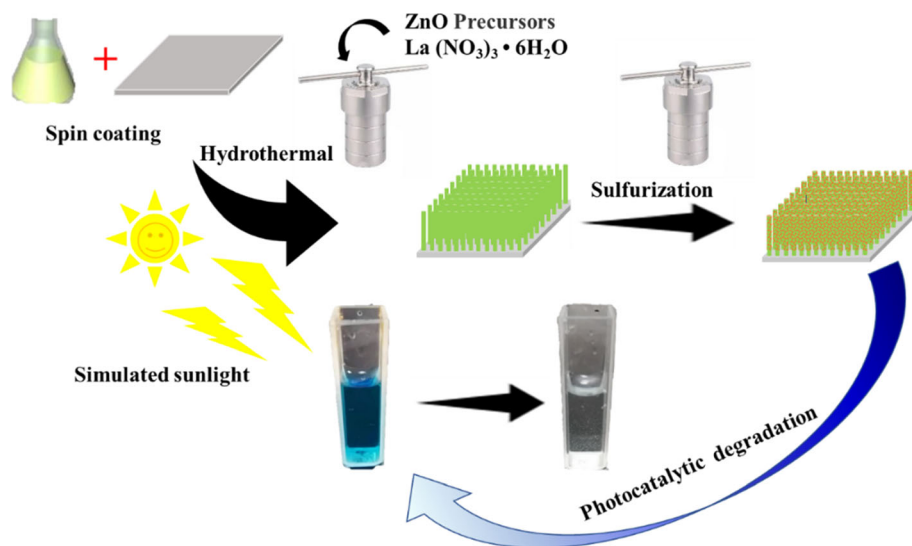
$$\eta = \left(1 - \frac{C}{C_0}\right) \times 100\% \quad (1)$$

where “ $C$ ” is the MB solution concentration at time “ $t$ ,” and “ $C_0$ ” is the initial MB solution concentration.

### Results and discussion

Figure 3a, b shows the XRD diffraction pattern of the samples, from which it can be seen that all the undoped ZnO nanorods, La-doped ZnO nanorods and ZnO/ZnS series composite samples show the hexagonal wurtzite structure of ZnO (JCPDS No. 79-

**Figure 2** Schematic diagram of photocatalyst preparation process.



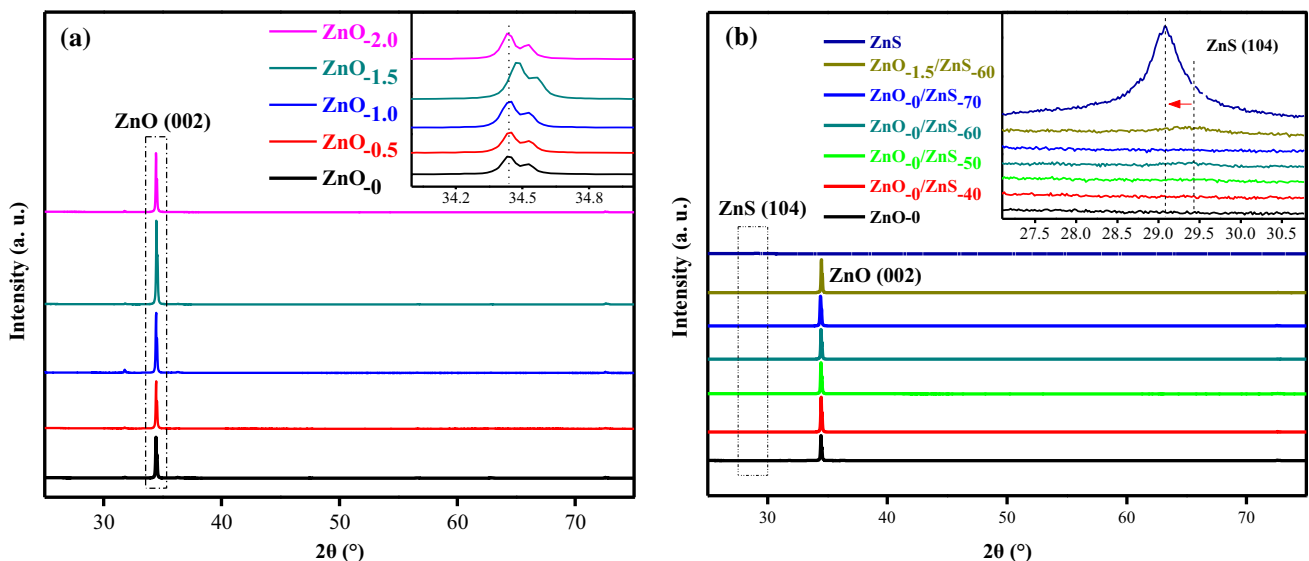
2205). Figure 3a shows the XRD diffraction pattern of the La-doped ZnO nanorods series samples. The sharp and strong ZnO (002) peak at about  $34^\circ$  indicates that all the samples have good crystal quality and preferred growth in (002) direction. In addition, as indicated in the inset of Fig. 3a, the (002) peak shifts significantly to the right, which indicates that La doping leads to the lattice shrinkage of ZnO crystal according to Bragg's law. The crystallite size of the samples was calculated by Debye–Scherrer formula with the full width at half maximum (FWHM) of ZnO (002) peak, and is listed in Table 1. When the La doping concentration is 1.5%, the ZnO crystallite size is the smallest due to heavy lattice shrinkage. However, compared with the undoped ZnO nanorods sample, when the La doping concentration is as high as 2.0%, excessive La atoms enter the interstitial positions of ZnO lattice and result in lattice expansion, which is indicated by the slight left shift of ZnO (002) peak. Therefore, the crystallite size of the ZnO<sub>-2.0</sub> sample is the biggest. Figure 3b shows the XRD diffraction pattern of the ZnO<sub>-c</sub>/ZnS<sub>-T</sub> series composite samples. A weak peak at about  $29.4^\circ$  in all the composite samples represents the (104) plane of hexagonal ZnS (JCPDS No. 72–0163), indicating that ZnS component was successfully synthesized in situ on the surface of ZnO nanorods. While in the ZnS sample, the peak becomes only slightly stronger and shifts to the left, indicating the degraded crystal quality and heavy lattice distortion due to high

concentration defects. Debye–Scherrer formula was used to calculate the crystallite size ( $D$ ) of the samples according to the FWHM of ZnO (002) peak:

$$D = K\lambda/B \cos \theta \quad (2)$$

where “ $K$ ” is a constant, “ $\lambda$ ” is the incident X-ray wavelength, “ $\theta$ ” is diffraction angle, and “ $B$ ” is FWHM.

The morphology of the samples was investigated with SEM measurements, as shown in Fig. 4. Figure 4a–e shows the morphology of the ZnO<sub>-c</sub> series samples. The image of the undoped ZnO nanorods sample in Fig. 4a shows that the orientation of the nanorods with an average diameter less than 100 nm is not very orderly. La doping increases the diameter of ZnO nanorods and makes them more ordered. The higher the La doping concentration, the larger the average diameter of the ZnO nanorods. When the doping concentration reaches 2.0%, the nanorods in the ZnO<sub>-2.0</sub> sample becomes very thick, with an average diameter of more than a few hundred nanometers, and the nanorods are even squeezed together. The results are consistent with the previous XRD measurements. Figure 4f–j shows the morphology of the ZnO<sub>-0</sub>/ZnS<sub>-T</sub> series samples, from which it can be seen that the sulfurization process does not significantly affect the morphology of the samples. Figure 4k–l shows the EDXS measurements of the ZnO<sub>-0</sub>/ZnS<sub>-60</sub> sample. O, Zn, Si and S elements are

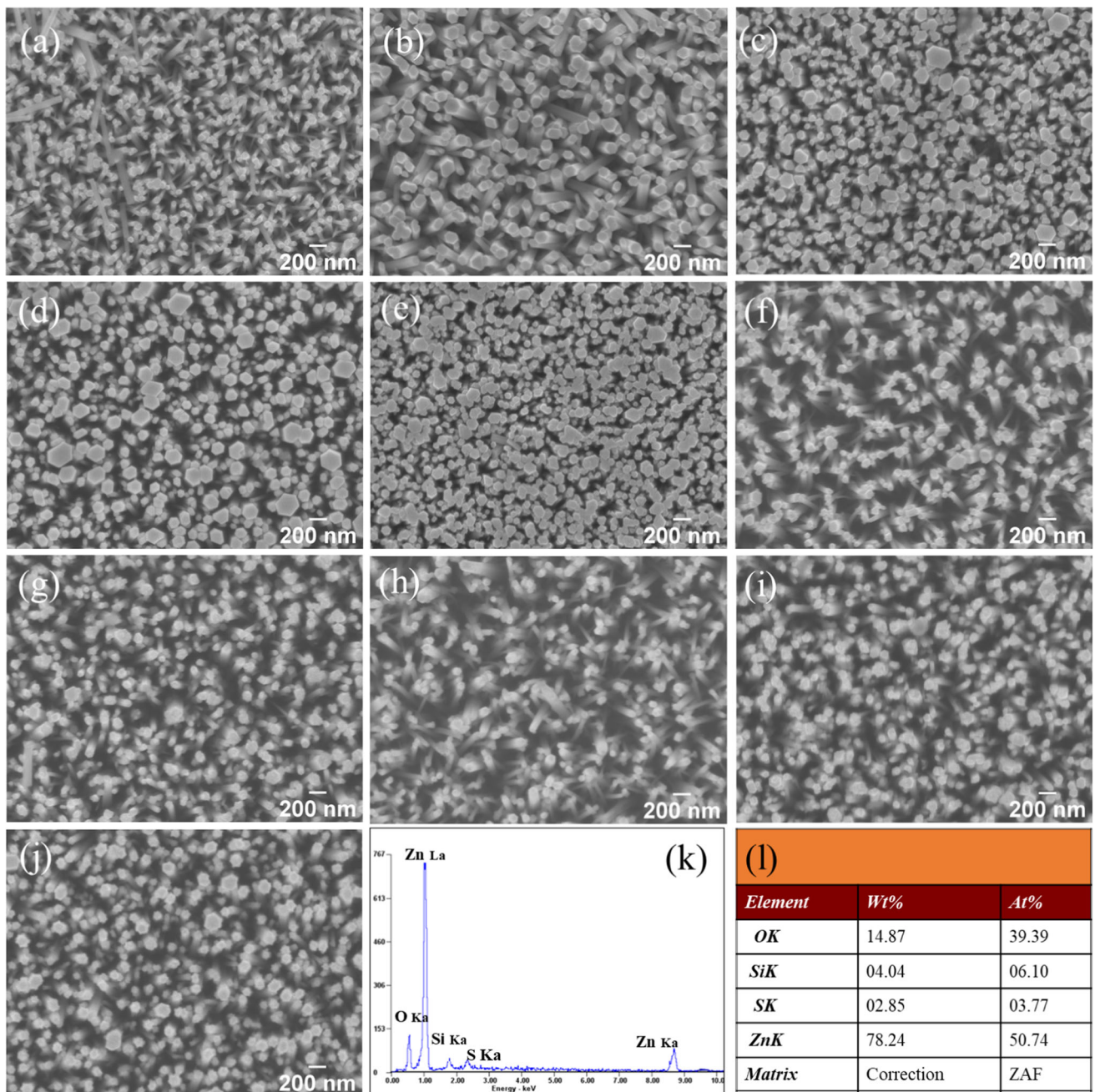


**Figure 3** XRD patterns of the samples: **a** ZnO<sub>-c</sub> series samples and **b** ZnO<sub>-c</sub>/ZnS<sub>-T</sub> series samples (The inset is the local enlargement of the part surrounded by dotted line in each figure).



**Table 1** FWHM and crystallite size of the ZnO<sub>c</sub> series samples

	ZnO <sub>0</sub>	ZnO <sub>0.5</sub>	ZnO <sub>1.0</sub>	ZnO <sub>1.5</sub>	ZnO <sub>2.0</sub>
FWHM(°)	0.14743	0.14978	0.14843	0.15604	0.1454
Crystallite Size (D/nm)	53.7958	52.9511	53.4332	50.8220	54.5472

**Figure 4** SEM images of the samples: **a–e** ZnO<sub>c</sub> series samples ( $c = 0, 0.5, 1.0, 1.5$  and  $2.0$ , respectively), **f–i** ZnO<sub>0</sub>/ZnS<sub>T</sub> series samples ( $T = 40, 50, 60$  and  $70$ , respectively), **j** Surface scanning

area of the ZnO<sub>1.5</sub>/ZnS<sub>60</sub> sample, and **k–l** Element distribution of the ZnO<sub>0</sub>/ZnS<sub>60</sub> sample.

detected, in which Si element comes from the substrate. The existence of S element further confirms the successful sulfurization of ZnO nanorods, which is also consistent with the XRD measurement results.

The TEM and EDXS measurements of the ZnO<sub>-1.5</sub>/ZnS<sub>-60</sub> sample are shown in Fig. 5. As shown in Fig. 5a, c, the TEM measurements show that the diameter of the nanorods is about 100 nm. The crystal plane spacing of 0.274 nm in Fig. 5b and 0.318 nm in Fig. 5d corresponds to the ZnO (100) and ZnS (104) planes, respectively, confirming the successful sulfurization of the ZnO nanorods in the ZnO<sub>-1.5</sub>/ZnS<sub>-60</sub> sample. In addition, as shown in Fig. 5c, the obtained ZnS nanoparticles with an average size of 40 nm are sparsely distributed on the surface of Zn nanorods, which contributes to the weak ZnS (104) diffraction peak intensity in Fig. 3. Figure 5e shows the selected area of the ZnO<sub>-1.5</sub>/ZnS<sub>-60</sub> sample for EDXS measurements, and Fig. 5f–j shows the element mapping of Zn, O, S, La, Si elements, indicating the uniform distribution of the elements, where Si element comes from the substrate.

The optical absorption characteristics of the samples were studied by UV–vis absorption spectroscopy. As shown in Fig. 6, the ZnO<sub>-c</sub> and ZnO<sub>-c</sub>/ZnS<sub>-T</sub> series samples show high absorbance in the ultraviolet region of about 400 nm, which comes from the intrinsic absorption of ZnO. In Fig. 6a, all the samples except the ZnO<sub>-0</sub> show high absorbance in the visible light region of 400–600 nm, which is attributed to the increase in V<sub>O</sub> defect concentration in ZnO crystal [31]. Because the electronegativity of La (1.10) is lower than that of Zn (1.65), the intrinsic absorbance of La-doped ZnO is red-shifted [32, 33]. Simultaneously, due to the introduction of a large number of defects caused by La doping, impurity energy levels are formed in ZnO band structure, which improves the visible light absorption of the ZnO<sub>-c</sub> series samples. The visible light absorbance of the ZnO<sub>-c</sub> series samples first increases and then decreases with the increase in La doping concentration, and the maximum value appears in the ZnO<sub>-1.5</sub> sample. Figure 6b shows the absorbance of the ZnO<sub>-c</sub>/ZnS<sub>-T</sub> series samples. In the undoped composite samples, the absorbance of the samples increases first and then decreases in visible light region with the increase in sulfurization time, and the maximum value appears in the ZnO<sub>-0</sub>/ZnS<sub>-60</sub> sample. Considering the high visible light absorption in the ZnS sample caused by S-related defects [34], the increase

in visible light absorption of the ZnO<sub>-0</sub>/ZnS<sub>-T</sub> series samples seems to be due to the increase in ZnS content in the composites. However, the visible light absorption of the ZnO<sub>-0</sub>/ZnS<sub>-70</sub> sample with higher ZnS content decreases. Therefore, the increase in visible light absorption of the ZnO<sub>-0</sub>/ZnS<sub>-T</sub> series samples may be attributed to another possibility of the separation efficiency of photo-generated electron–hole pairs in the heterojunctions. Therefore, the decrease in visible light absorption of the ZnO<sub>-0</sub>/ZnS<sub>-70</sub> can be explained by the decrease in the separation efficiency of photo-generated electron–hole pairs due to the formation of excessive ZnS in the composite. In addition, the visible light absorption of the ZnO<sub>-1.5</sub>/ZnS<sub>-60</sub> is higher than that of the ZnO<sub>-0</sub>/ZnS<sub>-60</sub> due to La doping.

As shown in Fig. 6c, the fitting optical band gap (E<sub>g</sub>) of the samples was calculated by Tauc formula, and the obtained values of the samples are listed in Table 2. Tauc formula is as follows [35, 36]:

$$(\alpha h\nu)^{1/n} = A(h\nu - E_g) \quad (3)$$

where “ $\alpha$ ” is the absorption coefficient, “ $A$ ” is the constant, and “ $h\nu$ ” is incident light energy. For direct transition semiconductor, “ $n$ ” is “1/2,” while for indirect transition semiconductor, “ $n$ ” is “2.”

The PL spectra of the samples are shown in Fig. 7. The ZnO intrinsic emission peak at about 390 nm appears in all the composite samples. And the peak at about 460 nm is attributed to the emission associated with oxygen vacancy (V<sub>O</sub>) defects. Figure 7a shows that La doping improves the intrinsic emission intensity of ZnO, indicating the improvement of ZnO crystal quality, which is consistent with the XRD measurement results. As shown in Fig. 7b, the intrinsic emission intensity of ZnO decreases gradually with the increase in sulfurization time in the ZnO<sub>-0</sub>/ZnS<sub>-T</sub> series samples, implying that ZnO/ZnS heterojunction is formed by the formation of ZnS component. Considering that both ZnO and ZnS are n-type semiconductors, due to the potential difference of the conduction band minimum (CBM) between ZnO and ZnS, a built-in electric field from ZnO to ZnS is formed at the interface when ZnO and ZnS form a heterojunction, which promotes the separation of photo-generated electron–hole pairs and prolongs carrier lifetime. Therefore, with the increase in sulfurization time, the ZnS content in ZnO/ZnS composite increases and the recombination of photo-generated electrons and holes is inhibited. In



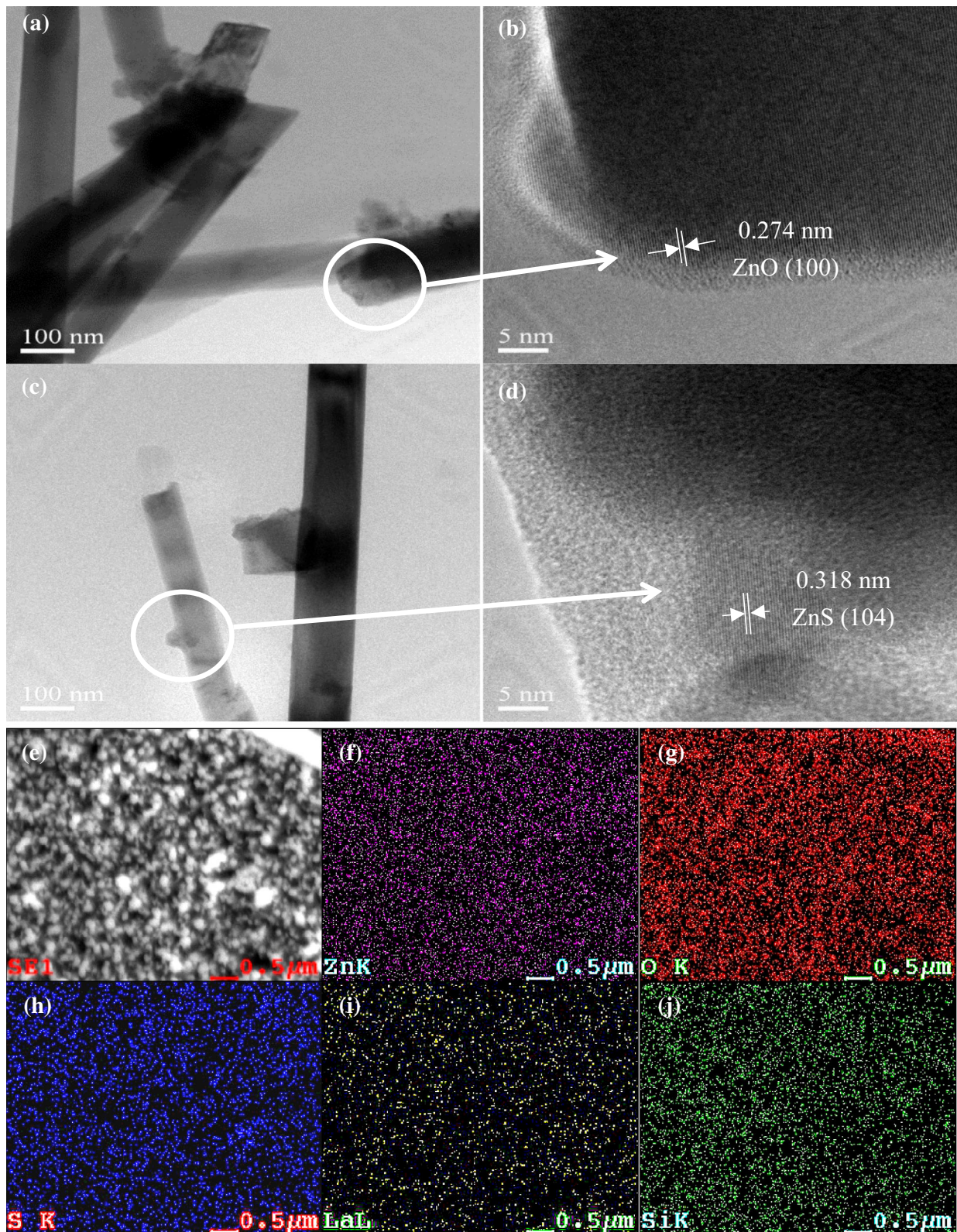


**Figure 5** Composition and element distribution measurements of the ZnO<sub>0.15</sub>/ZnS<sub>0.60</sub> sample: **a-d** TEM measurements, **e** Selected area for EDXS measurements and **f-j** Element mapping of Zn, O, S, La and Si elements.



addition, compared with the ZnO<sub>0</sub>/ZnS<sub>60</sub> sample, the ZnO intrinsic emission intensity of the ZnO<sub>1.5</sub>/ZnS<sub>60</sub> sample is greatly increased, which may be due to two possibilities. One is that La doping increases carrier concentration, and the other is that the original Z-scheme electron transport mechanism in the heterojunction is changed to type-II. In addition, as shown in Fig. 7b, with the increase in sulfurization

time, the intrinsic emission intensity of ZnO in the undoped composite samples becomes lower and lower, and the lowest value appears in the ZnO<sub>0</sub>/ZnS<sub>60</sub> sample, indicating that the number of ZnO CB electrons falling back to the VB becomes less, which is attributed to the separation of photo-generated carrier in heterojunction [30]. However, the ZnO intrinsic emission intensity in the ZnO<sub>1.5</sub>/ZnS<sub>60</sub> sample is

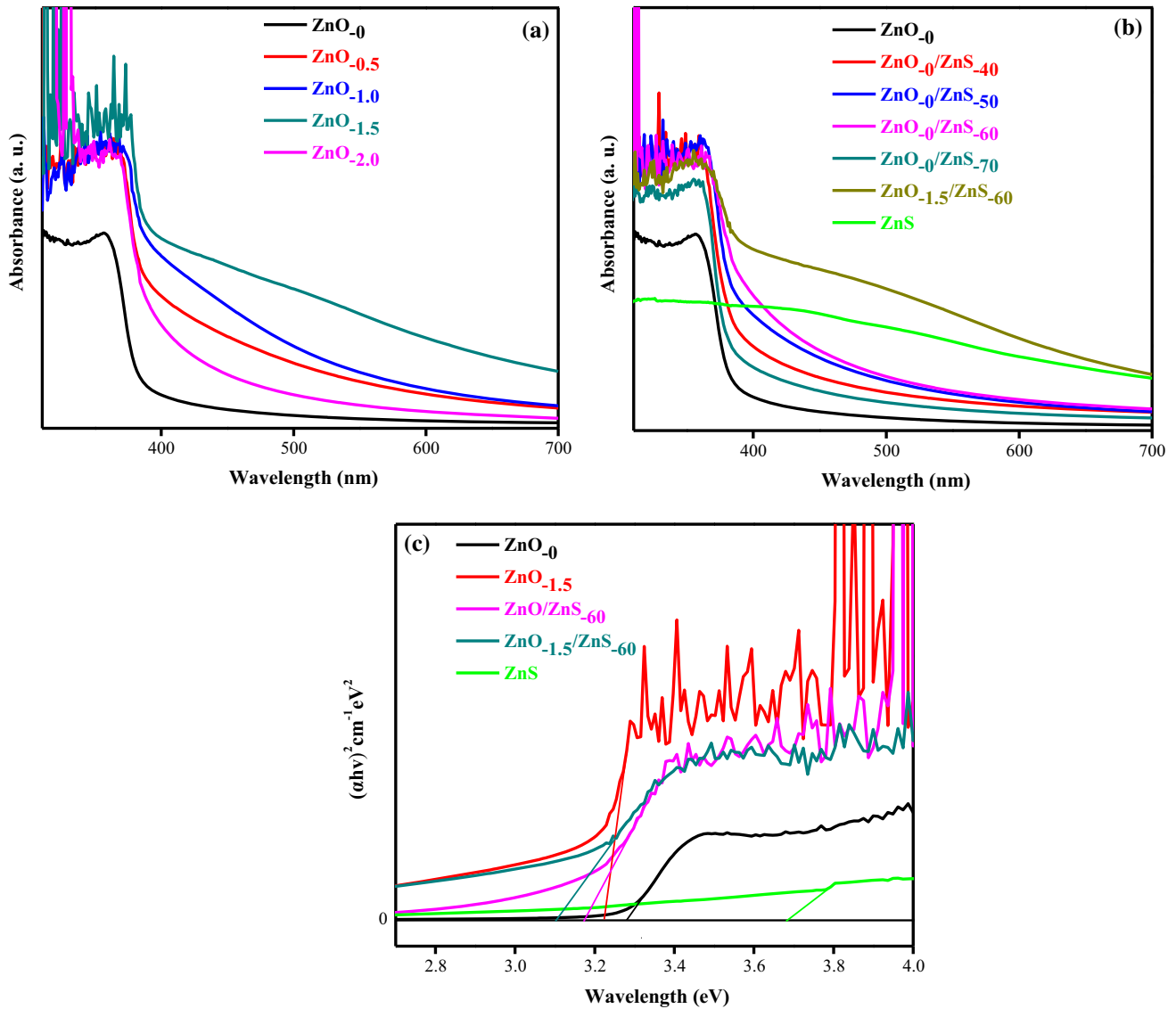


**Figure 6** UV–vis measurements of the samples: **a** ZnO<sub>c</sub> series samples, **b** ZnO<sub>0</sub>, ZnS and ZnO<sub>c</sub>/ZnS<sub>T</sub> series samples, and **c** Tauc plots of the ZnO<sub>0</sub>, ZnO<sub>1.5</sub>, ZnO<sub>0</sub>/ZnS<sub>60</sub>, ZnO<sub>1.5</sub>/ZnS<sub>60</sub> samples.

**Table 2** Optical band gaps of the ZnO<sub>0</sub>, ZnO<sub>1.5</sub>, ZnO<sub>0</sub>/ZnS<sub>60</sub>, ZnO<sub>1.5</sub>/ZnS<sub>60</sub> and ZnS samples

Sample ID	ZnO <sub>0</sub>	ZnO <sub>1.5</sub>	ZnO <sub>0</sub> /ZnS <sub>60</sub>	ZnO <sub>1.5</sub> /ZnS <sub>60</sub>	ZnS
Optical band gap (E <sub>g</sub> )	3.28 eV	3.22 eV	3.17 eV	3.10 eV	3.68 eV

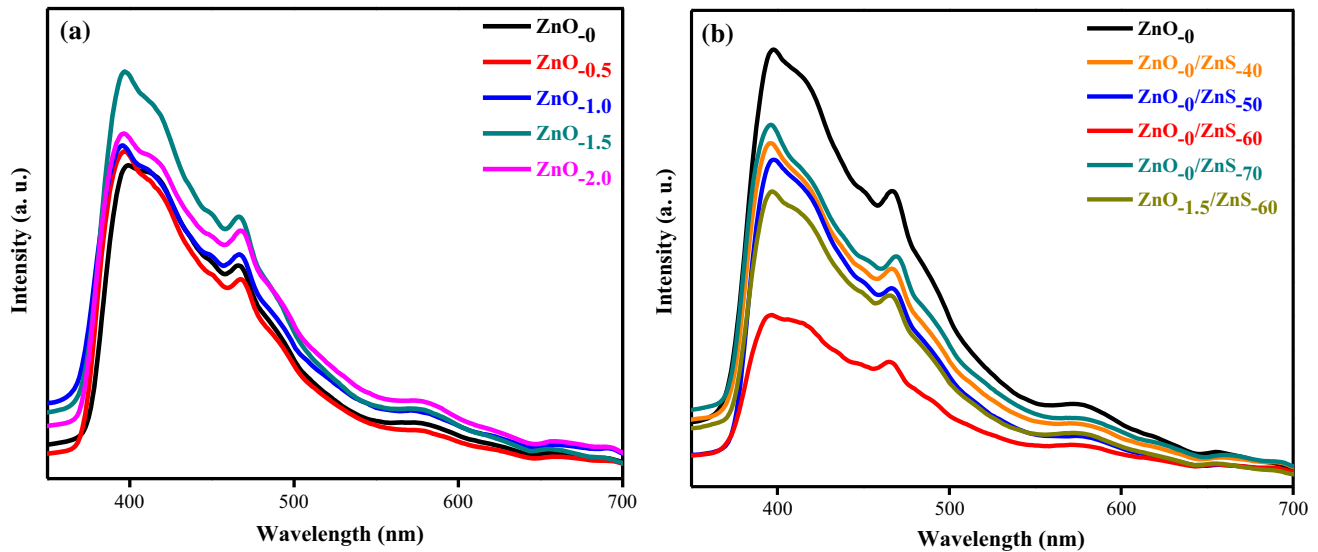


**Figure 7** PL spectra of the samples: **a**  $\text{ZnO}_c$  series samples, and **b**  $\text{ZnO}_c/\text{ZnS}_T$  series samples.

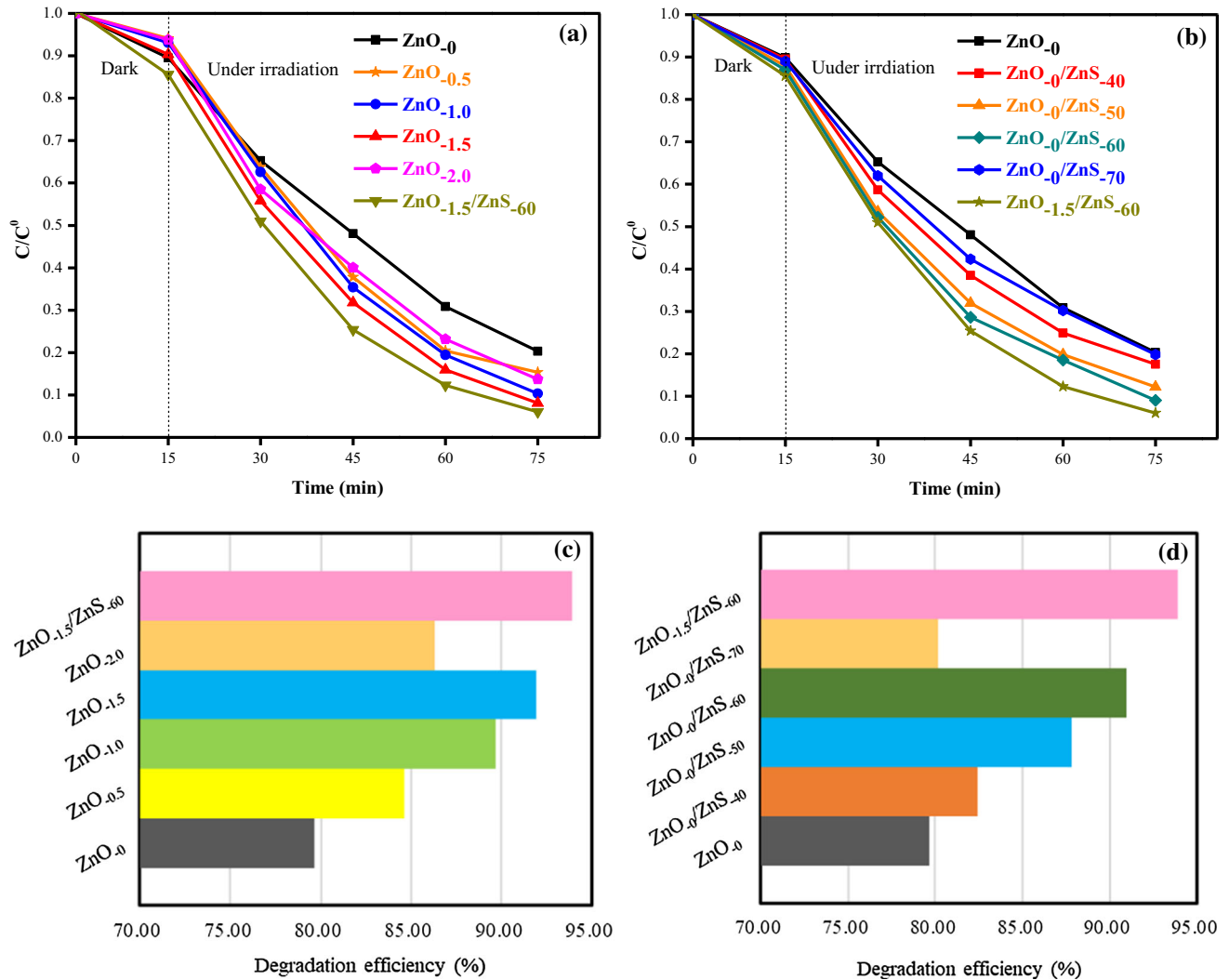
much higher than that in the  $\text{ZnO}_0/\text{ZnS}_{60}$  sample, which may be caused by the decrease in carrier mobility caused by heavy doping in the  $\text{ZnO}_{-1.5}/\text{ZnS}_{60}$  sample. For Z-scheme carrier transfer mechanism in  $\text{ZnO}/\text{ZnS}$  heterojunction, the electrons in the CB of  $\text{ZnO}$  are transferred to the VB of  $\text{ZnS}$  and combined with the holes there, leaving holes in the VB of  $\text{ZnO}$  and electrons in the CB of  $\text{ZnS}$ . While for type-II carrier transfer mechanism in  $\text{ZnO}/\text{ZnS}$  heterojunction, carrier transport direction depends on cascade band structure of the composite. If the carrier transfer mechanism in the  $\text{ZnO}_{-1.5}/\text{ZnS}_{60}$  sample is changed from Z-scheme to type-II, more electrons in the CB of  $\text{ZnO}$  can fall to the VB of  $\text{ZnO}$  and combine with the holes there. Then, the increase in  $\text{ZnO}$  intrinsic emission intensity is possible.

Figure 8 shows the photocatalytic activity of the samples, which is characterized by the degradation efficiency of MB solution under simulated sunlight. The MB solution containing the sample to be tested was first placed in the dark for 15 min to obtain the molecular adsorption and desorption equilibrium on its surface, and then irradiated with simulated sunlight for 60 min. By tracking the intrinsic absorbance change of the MB solution at 665 nm wavelength, the concentration change of the MB solution caused by the photocatalytic behavior of the sample can be determined. In Figure 8a, compared with the  $\text{ZnO}_0$  sample, the degradation efficiency of the  $\text{ZnO}_c$  series samples is much improved. And it increases first and then decreases with the increase in La doping

concentration, and the maximum value appears in the  $\text{ZnO}_{-1.5}$  sample. However, compared with the  $\text{ZnO}_{-1.5}$  sample, the  $\text{ZnO}_{-1.5}/\text{ZnS}_{60}$  composite sample shows better photocatalytic performance due the separation of photo-generated electron–hole pairs. Figure 8b shows the photocatalytic performance of the  $\text{ZnO}_c/\text{ZnS}_T$  series samples, which first increases and then decreases with sulfurization time, and the maximum value appears in the  $\text{ZnO}_0/\text{ZnS}_{60}$  sample. In addition, although the  $\text{ZnO}_0/\text{ZnS}_{60}$  sample shows the best photocatalytic performance in the  $\text{ZnO}_c/\text{ZnS}_T$  series samples, the performance of the  $\text{ZnO}_{-1.5}/\text{ZnS}_{60}$  sample seems to be better than it due to La doping. Figure 8c, d shows the photocatalytic performance comparison of the samples, and the detailed values are listed in Table 3.

Figure 9 shows the pseudo-first-order reaction rate constant of MB solution photocatalyzed by the samples. Figure 9a, b shows the fitting degradation kinetic curves of MB solution photocatalyzed by the  $\text{ZnO}_c$  and  $\text{ZnO}_c/\text{ZnS}_T$  series samples, respectively. Generally, the time dependence of  $\ln(C_0/C)$  is approximately linear, and the slope of the fitting line is described as degradation rate constant ( $K$ ). Therefore, the detailed degradation rate constants of MB solution photocatalyzed by the  $\text{ZnO}_c$  and  $\text{ZnO}_c/\text{ZnS}_T$  series samples are shown in Fig. 9c, d, and the highest value of 0.03916 is for the  $\text{ZnO}_{-1.5}/\text{ZnS}_{60}$  sample (Table 4).

Figure 10 shows the performance stability test of the  $\text{ZnO}_{-1.5}/\text{ZnS}_{60}$  sample in the cyclic photocatalytic



**Figure 8** Photocatalytic characteristics of the samples to MB solution: **a**  $ZnO_{-c}$  series samples, **b**  $ZnO_{-c}/ZnS_{-T}$  series samples and **c**, **d** Degradation rate constants of MB solution photocatalyzed by the samples.

degradation of MB solution. As shown in Fig. 10a, after four cyclic tests, the degradation efficiency of MB solution still remains at 90.25%, indicating good stability of the sample. In addition, the structural

stability of the sample is also investigated with XRD measurements. As shown in Fig. 10b, the sample structure does not change after four cyclic tests, and even the intensity of ZnO (002) peak does not change

**Table 3** Degradation rate constants of MB solution photocatalyzed by the  $ZnO_{-c}$  and  $ZnO_{-c}/ZnS_{-T}$  series samples, respectively

Sample ID	Degradation efficiency of MB solution (%)	Sample ID	Degradation efficiency of MB solution (%)
$ZnO_{-0}$	79.66	$ZnO_{-0}$	79.66
$ZnO_{-0.5}$	84.65	$ZnO_{-0}/ZnS_{-40}$	82.45
$ZnO_{-1.0}$	89.65	$ZnO_{-0}/ZnS_{-50}$	87.80
$ZnO_{-1.5}$	91.92	$ZnO_{-0}/ZnS_{-60}$	90.99
$ZnO_{-2.0}$	86.29	$ZnO_{-0}/ZnS_{-70}$	80.18
$ZnO_{-1.5}/ZnS_{-60}$	93.92	$ZnO_{-1.5}/ZnS_{-60}$	93.92



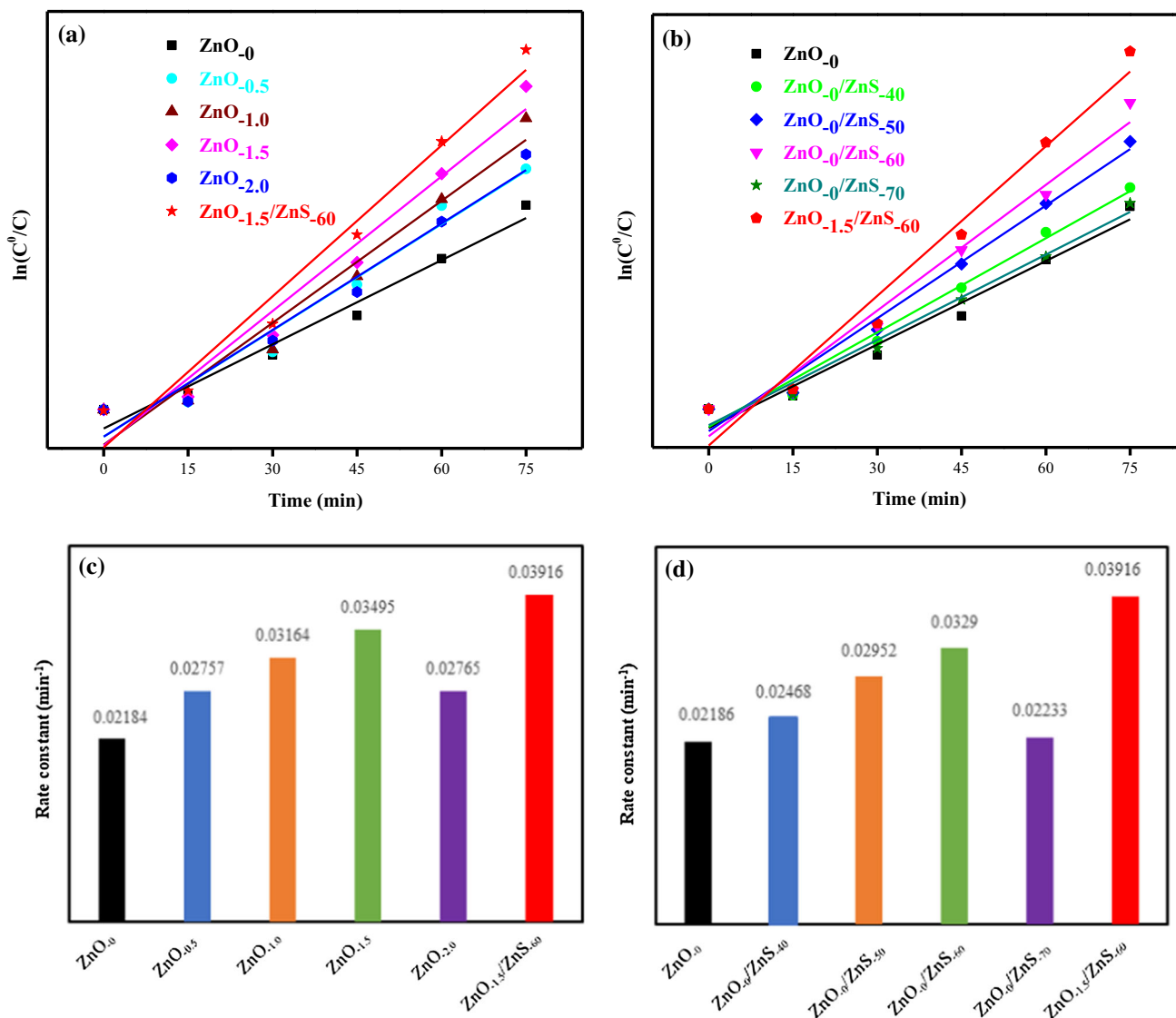


**Figure 9** Photocatalytic performance of the ZnO<sub>c</sub> and ZnO<sub>c</sub>/ZnS<sub>T</sub> series samples for MB solution: **a, b** Fitting degradation rate curves and **c, d** Degradation rate constants of the ZnO<sub>c</sub> and ZnO<sub>c</sub>/ZnS<sub>T</sub> series samples, respectively.

**Table 4** Degradation rate constants of MB solution photocatalyzed by the ZnO<sub>c</sub> and ZnO<sub>c</sub>/ZnS<sub>T</sub> series samples

Sample ID	Rate constant	Sample ID	Rate constant
ZnO <sub>0</sub>	0.0218	ZnO <sub>0</sub>	0.0218
ZnO <sub>0.5</sub>	0.0275	ZnO <sub>0</sub> /ZnS <sub>40</sub>	0.0246
ZnO <sub>1.0</sub>	0.0316	ZnO <sub>0</sub> /ZnS <sub>50</sub>	0.0295
ZnO <sub>1.5</sub>	0.0349	ZnO <sub>0</sub> /ZnS <sub>60</sub>	0.0329
ZnO <sub>2.0</sub>	0.0276	ZnO <sub>0</sub> /ZnS <sub>70</sub>	0.0223
ZnO <sub>1.5</sub> /ZnS <sub>60</sub>	0.0391	ZnO <sub>1.5</sub> /ZnS <sub>60</sub>	0.0391

visibly, indicating that the ZnO<sub>1.5</sub>/ZnS<sub>60</sub> sample has good structural stability in photocatalytic degradation process.

The surface element binding states of the samples are studied with the X-ray photoelectron spectroscopy (XPS) measurements for the ZnO<sub>0</sub>, ZnO<sub>1.5</sub>, ZnO<sub>0</sub>/ZnS<sub>60</sub> and ZnO<sub>1.5</sub>/ZnS<sub>60</sub> samples. As shown in Fig. 11a, Zn, O, S, and La elements are confirmed in the ZnO<sub>1.5</sub>/ZnS<sub>60</sub> sample. Figure 11b shows Zn 2p binding energy of the samples. For the ZnO<sub>0</sub> sample, the peaks at 1042.17 eV and 1019.11 eV correspond to Zn 2p<sub>1/2</sub> and Zn 2p<sub>3/2</sub> states, respectively. The energy difference between the two peaks is 23.06 eV, indicating that Zn element exists in the oxidation state of Zn<sup>2+</sup> [36]. Compared with the ZnO<sub>0</sub> sample, the peak positions of Zn 2p in the ZnO<sub>0</sub>/ZnS<sub>60</sub> sample shift slightly to the direction of low

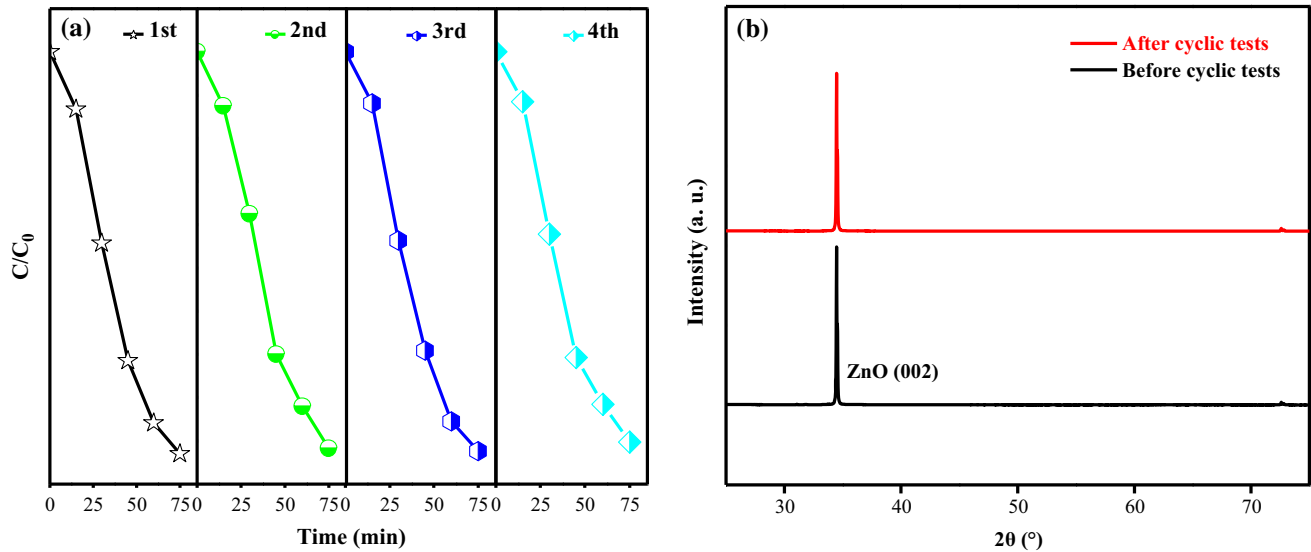


**Figure 10** Four cyclic degradation tests of MB solution photocatalyzed by the  $\text{ZnO}_{0.15}/\text{ZnS}_{0.60}$  sample: **a** Change of degradation efficiency in each test and **b** Change of the sample structure before and after four cyclic degradation tests.

binding energy, which may be induced by the lower electronegativity of S atom (2.58) than O atom (3.44). Furthermore, another factor leading to the peak shift cannot be ignored, that is, free charges migrate through the interface in heterojunction and form a built-in electric field in the  $\text{ZnO}_0/\text{ZnS}_{0.60}$  sample [37, 41]. The XRD, SEM and TEM measurements confirm a fact that ZnS content in all the composite samples is very low, and then  $\text{Zn}^{2+}$  ions mainly come from the ZnO component in the composites [1]. Therefore, if the low energy direction peak shift of Zn 2p is caused by the built-in electric field in the  $\text{ZnO}_0/\text{ZnS}_{0.60}$  composite sample, the built-in electric field direction can be deduced from the ZnS component to the ZnO component. Compared with the  $\text{ZnO}_{0.15}$  sample, two Zn 2p peaks in the  $\text{ZnO}_{0.15}/\text{ZnS}_{0.60}$  sample shift to the direction of high binding energy, which illustrates that the number of free charges in the ZnO component becomes more due to La donor doping, the increase in Fermi level in the La-doped ZnO component promotes free charges to migrate to ZnS component in the heterojunction [38, 39], and the direction of the built-in electric field in the heterojunction is from the ZnO component to the ZnS component, which is opposite to that in the  $\text{ZnO}_0/\text{ZnS}_{0.60}$  sample. The results show that the peak shift direction of the element binding energy in the composites is dominated by the free charge migration direction through the interface between the two components, rather than by the electronegativity

difference between S and O atoms. In addition, compared with the  $\text{ZnO}_0$  sample, the Zn 2p peak positions in the  $\text{ZnO}_{0.15}$  sample shift slightly to the direction of low binding energy, which is due to the fact that the electronegativity of La atom (1.10) is lower than that of Zn atom (1.65). In Fig. 11c, O element binding state in the  $\text{Zn}_0$  sample can be fitted into three peaks of 527.87 eV (I), 529.39 eV (II), and 530.60 eV (III), which correspond to the lattice oxygen atom,  $\text{O}_V$  defect, and surface adsorbed oxygen, respectively [38–41]. Compared with the  $\text{Zn}_0$  sample, the peak II intensity decreases and the peak I intensity increases in the  $\text{Zn}_0/\text{ZnS}_{0.60}$  sample, which illustrate that the free charge transfer from the ZnS component to the ZnO component in the composite reduces the concentration  $\text{V}_O$  defects and increases the concentration of lattice oxygen atoms. In addition, compared with the  $\text{ZnO}_0$  sample, the obtained free charges make the peak II and peak III in the  $\text{Zn}_0/\text{ZnS}_{0.60}$  sample shift to the direction of low binding energy. In the composite, although the ZnO component obtains free charges from the ZnS component, the decrease in  $\text{V}_O$  defect concentration and the increase in lattice oxygen atom concentration make the peak I move slightly to the direction of high binding energy. Moreover, for the  $\text{ZnO}_{0.15}/\text{ZnS}_{0.60}$  sample discussed above, La donor doping introduces a large number of free charges into the ZnO component in the sample, which leads to an increase in ZnO Fermi level. Therefore, the migration of free charges

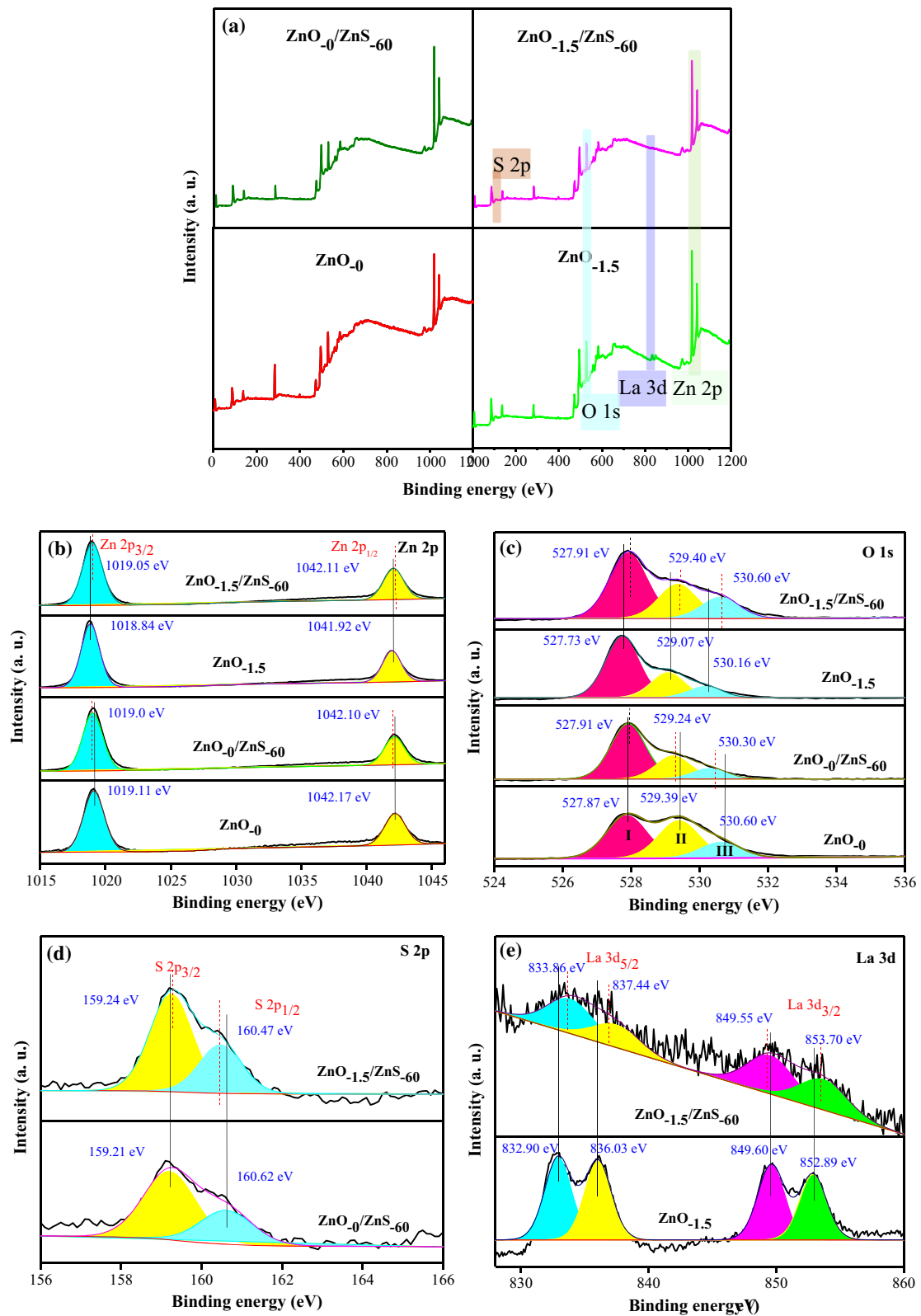


**Figure 11** XPS diffraction spectra of the  $\text{ZnO}_{-0}$ ,  $\text{ZnO}_{-1.5}$ ,  $\text{ZnO}_{-0}/\text{ZnS}_{-60}$ , and  $\text{ZnO}_{-1.5}/\text{ZnS}_{-60}$  samples: **a** Full spectra of the samples and **b–e** High-resolution spectra of Zn 2p, O 1s, S 2p and La 3d in the samples.



from ZnO to ZnS forms a built-in electric field from the ZnO component to the ZnS component in the sample. In Fig. 11c, compared with the ZnO<sub>-1.5</sub> sample, the high-energy direction shift of the O 1s binding states (indicated by the Peak I, Peak II and Peak III) is caused by the free charge transfer from the ZnO component to the ZnS component. Figure 11d shows that in the ZnO<sub>0</sub>/ZnS<sub>60</sub> sample, the binding peaks of S 2p<sub>1/2</sub> and S 2p<sub>3/2</sub> are located at 160.62 eV and 159.21 eV, respectively, while in the ZnO<sub>-1.5</sub>/ZnS<sub>60</sub> sample, the binding peaks of S 2p<sub>1/2</sub> and S 2p<sub>3/2</sub> are located at 160.47 eV and 159.24 eV respectively. Compared with the ZnO<sub>0</sub>/ZnS<sub>60</sub> sample, the peak shift of S 2p<sub>1/2</sub> and S 2p<sub>3/2</sub> in the ZnO<sub>-1.5</sub>/ZnS<sub>60</sub> sample illustrates that the La doping concentration in ZnO affects the elemental binding states in the ZnO/ZnS-based composites, and may even affect the carrier transfer mechanism in the heterojunctions. Figure 11e illustrates that the binding energies of La 3d<sub>3/2</sub> and La 3d<sub>5/2</sub> are detected in both of the ZnO<sub>-1.5</sub> and ZnO<sub>-1.5</sub>/ZnS<sub>60</sub> samples [42, 43]. Compared with the ZnO<sub>-1.5</sub> sample, the La 3d binding peaks in the ZnO<sub>-1.5</sub>/ZnS<sub>60</sub> sample shift to the direction of high energy, which confirms a fact that the free charges in the ZnO component are transferred to the ZnS component through the interface and a built-in electric field is formed in the heterojunction.

According to Mott–Schottky equation, the carrier density (N<sub>D</sub>) of the samples can be calculated. The Mott–Schottky plots (M-S plot) of the samples are shown in Fig. 12, by which the flat band potentials (E<sub>FB</sub>) of the samples are obtained. Mott–Schottky equation is as follows [44, 45]:

$$1/C_s^2 = (2/q\epsilon\epsilon_0N_D)[(E_{AP} - E_{FB}) - KT/q] \tag{4}$$

$$N_D = (2/q\epsilon\epsilon_0)[d(1/C_s^2)/dE]^{-1} \tag{5}$$

where “q” is elementary charge, “K” is the Boltzmann constant, “T” is the absolute temperature, “ε<sub>0</sub>” is the vacuum dielectric constant, “ε” is the dielectric constant of ZnO, “C<sub>s</sub>” is the capacitance of the space charge region per unit area of semiconductor, and “E<sub>AP</sub>” is the applied potential between the electrodes for M-S plot [38]. The Mott–Schottky equation is derived from plate electrodes, so the calculated “N<sub>D</sub>” and “E<sub>FB</sub>” values are only used for comparison purpose [46]. According to the Mott–Schottky plots, the E<sub>FB</sub> potentials of the ZnO<sub>0</sub>, ZnO<sub>-1.5</sub>, ZnO<sub>0</sub>/ZnS<sub>60</sub>, ZnO<sub>-1.5</sub>/ZnS<sub>60</sub> and ZnS samples are fitted with SCE as the reference potential in Fig. 12. The detailed

values are converted by using NHE as the reference potential and listed in Table 5. Since E<sub>FB</sub> can be regarded as the conduction band minimum potential (E<sub>CBM</sub>) approximately for n-type semiconductor, its valence band maximum potential (E<sub>VBM</sub>) can be calculated as follows:

$$E_{VBM} = E_g + E_{CBM} \tag{6}$$

where “E<sub>g</sub>” is the optical band gap of semiconductor. Therefore, the calculated results of the samples are also shown in Tab. 5. The positive fitting curve slope of the ZnO<sub>0</sub>, ZnO<sub>-1.5</sub>, ZnO<sub>0</sub>/ZnS<sub>60</sub>, ZnO<sub>-1.5</sub>/ZnS<sub>60</sub> and ZnS samples indicates that all the samples are n-type semiconductor. Since carrier density N<sub>D</sub> is inversely proportional to the slope of fitting line according to Eqs. (4) and (5), the carrier concentration in the ZnO<sub>-1.5</sub>/ZnS<sub>60</sub> sample is inferred to be the highest.

In order to further investigate the carrier transfer mechanism in ZnO/ZnS-based composite photocatalysts, the band structures of the ZnO<sub>0</sub>, ZnO<sub>-1.5</sub>, ZnO<sub>0</sub>/ZnS<sub>60</sub>, ZnO<sub>-1.5</sub>/ZnS<sub>60</sub> samples are shown in Fig. 13. The band structure change of ZnO after La doping is shown in Fig. 13a, in which the valence band of ZnO is mainly from the orbital levels of O 2p, and the conduction band is mainly from the orbital levels of Zn 4 s. When La element is doped in ZnO nanorods, the partial hybridization between the outermost electron orbitals of La element and the electron orbitals in ZnO conduction band produces an additional occupied shallow donor state, resulting in the narrowing of ZnO band gap [47]. In addition, La donor doping introduces more free electrons into ZnO, as shown in Fig. 12, making the Fermi level of the ZnO<sub>-1.5</sub> sample close to its CB. For the same reason, the electron binding energy of Zn and O elements in the ZnO<sub>-1.5</sub> sample decreases to a certain extent, as shown in Fig. 11. Thus, the overall band structure of the ZnO<sub>-1.5</sub> sample moves upward. Since the ZnO intrinsic absorbance in the ZnO<sub>0</sub>/ZnO<sub>60</sub> sample is higher than that in the ZnO<sub>0</sub> sample as shown in Fig. 6b and the ZnO intrinsic emission in the ZnO<sub>0</sub>/ZnS<sub>60</sub> sample is lower than that in the ZnO<sub>0</sub> sample as shown in Fig. 7 (b), it can be inferred that photo-generated electrons and holes are separated in the ZnO<sub>0</sub>/ZnS<sub>60</sub> sample. According to the band structures of the ZnO<sub>0</sub> and ZnO<sub>0</sub>/ZnO<sub>60</sub> samples shown in Fig. 13b, due to the band bending induced by the built-in electric field in the heterojunction, when the photo-generated electrons in the

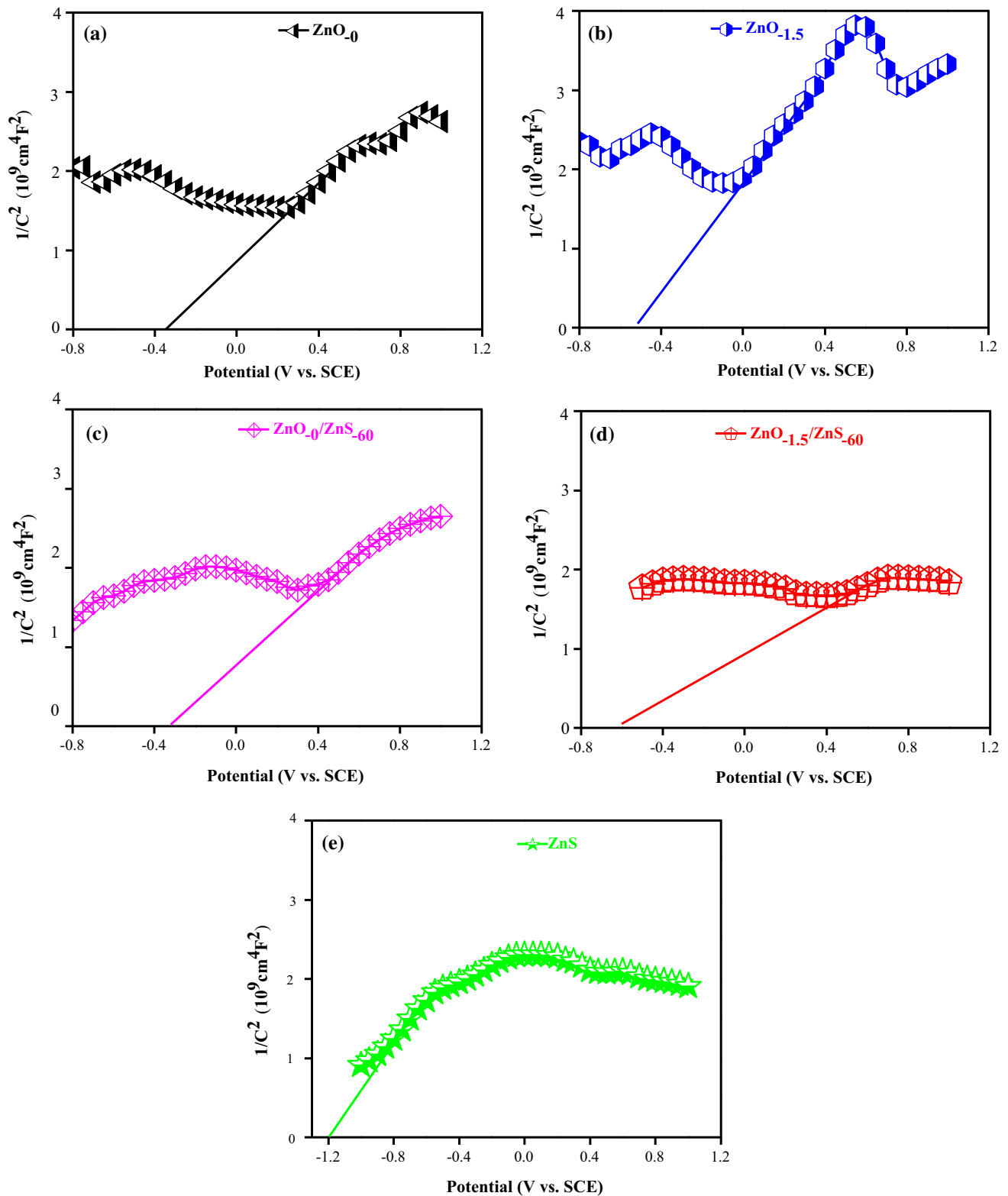


**Figure 12** Mott–Schottky plots of **a**  $\text{ZnO}_0$ , **b**  $\text{ZnO}_{-1.5}$ , **c**  $\text{ZnO}_0/\text{ZnS}_{60}$ , **d**  $\text{ZnO}_{-1.5}/\text{ZnS}_{60}$  and **e**  $\text{ZnS}$  samples.

**Table 5**  $E_{CBM}$ ,  $E_{VBM}$  and  $E_g$  values of the ZnO<sub>0</sub>, ZnO<sub>1.5</sub>, ZnO<sub>0</sub>/ZnS<sub>60</sub>, ZnO<sub>1.5</sub>/ZnS<sub>60</sub> and ZnS samples with NHE as the reference

Sample ID	$E_{CBM}$	$E_{VBM}$	$E_g$
ZnO <sub>0</sub>	- 0.09 V	+ 3.19 V	3.28 eV
ZnO <sub>1.5</sub>	- 0.26 V	+ 2.96 V	3.22 eV
ZnO <sub>0</sub> /ZnS <sub>60</sub>	- 0.06 V	+ 3.11 V	3.17 eV
ZnO <sub>1.5</sub> /ZnS <sub>60</sub>	- 0.36 V	+ 2.74 V	3.10 eV
ZnS	- 0.96 V	+ 2.72 V	3.68 eV

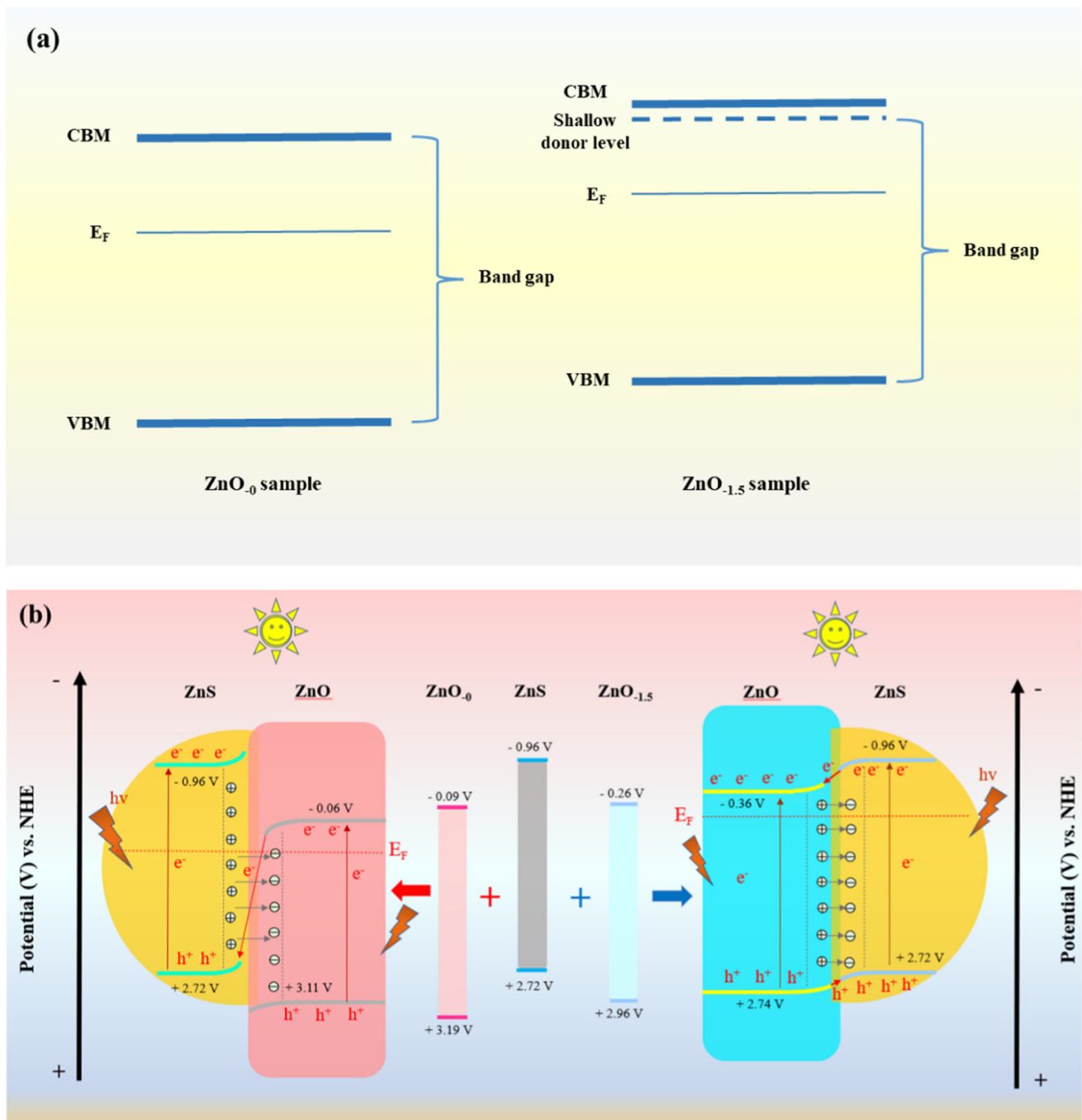


**Figure 13** Schematic diagram of band structure of the samples: **a** band structure change of ZnO caused by La donor doping and **b** band structures of the ZnO<sub>0</sub>, ZnO<sub>1.5</sub>, ZnS, ZnO<sub>0</sub>/ZnS<sub>60</sub> and ZnO<sub>1.5</sub>/ZnS<sub>60</sub> samples.



CB of ZnO are transferred between the components, they can only be transferred to the VB of ZnS and combine with the photo-generated holes there. Thus, the separation mechanism of photo-generated electron and hole pairs in the ZnO<sub>0</sub>/ZnS<sub>60</sub> sample can be clarified as a Z-scheme carrier transfer mechanism. When the sample is irradiated by light, the VB electrons of ZnO and ZnS are excited to their respective CBs. Some of the photo-generated electrons fall back to their respective CBs, contributing to the intrinsic emissions of ZnO and ZnS. Simultaneously, some of the CB electrons of ZnO are transferred to the VB of ZnS, and combined with the photo-generated holes there, leaving the electrons in the CB of ZnS and holes in the VB of ZnO. While in the ZnO<sub>1.5</sub>/ZnS<sub>60</sub> sample, the Fermi energy in ZnO is increased due to heavy La donor doping, and the free charges in the ZnO component are transferred to the ZnS component. Then, a new built-in electric field from ZnO to ZnS is formed in the heterojunction, and its direction is opposite to that of the ZnO<sub>0</sub>/ZnS<sub>60</sub> sample. The corresponding band bending forms a cascade band structure between the two components, as shown in Fig. 13b. Then, the photo-generated carrier transfer in the heterojunction follows a type-II mechanism, that is, the photo-generated electrons in the CB of ZnS are transferred to the CB of ZnO, and the photo-generated holes in the VB of ZnO are transferred to the VB of ZnS. The inference of type-II carrier transfer mechanism in the ZnO<sub>1.5</sub>/ZnS<sub>60</sub> sample is supported by the UV-vis and PL measurements.

In order to further study and clarify the photocatalytic reaction mechanism in the degradation of MB solution, the active group trapping experiments in photocatalytic reaction of MB solution were carried out on the ZnO, ZnO<sub>0</sub>/ZnS<sub>60</sub> and ZnO<sub>1.5</sub>/ZnS<sub>60</sub> samples under 75 min of Xe lamp irradiation. Triethanolamine (TEOA), isopropanol (IPA) and benzoquinone (BQ) were used as trapping agents to detect the contribution of photo-induced holes (h<sup>+</sup>), hydroxyl radicals (•OH) and superoxide radicals (•O<sub>2</sub>) to the degradation of MB solution, respectively [48–51]. The results are shown in Fig. 14. Since •O<sub>2</sub> group generation potential (O<sub>2</sub>/•O<sub>2</sub> vs. NHE, -0.33 V [12]) is lower than the CBM of ZnO (-0.09 V), •O<sub>2</sub> groups cannot be produced by the ZnO<sub>0</sub> sample. However, the introduction of ZnS component in the ZnO<sub>0</sub>/ZnS<sub>60</sub> and ZnO<sub>1.5</sub>/ZnS<sub>60</sub> samples modifies their band structure, and even provides a new transfer path for photo-generated carriers. Since the

CBM of ZnS (-0.96 V) in the ZnO<sub>0</sub>/ZnS<sub>60</sub> sample with Z-scheme carrier transfer mechanism is more negative than -0.33 V, the formation condition of •O<sub>2</sub> groups can be met in the ZnO<sub>0</sub>/ZnS<sub>60</sub> sample. For the ZnO<sub>1.5</sub>/ZnS<sub>60</sub> sample with type-II carrier transfer mechanism, the elevated CBM of ZnO (-0.36 V) due to La donor doping is also more negative than -0.33 V, and •O<sub>2</sub> groups can also be produced in the sample. These are the reasons why the •O<sub>2</sub> active groups produced by the ZnO<sub>0</sub>, ZnO<sub>0</sub>/ZnS<sub>60</sub> and ZnO<sub>1.5</sub>/ZnS<sub>60</sub> samples have different contributions to the degradation of MB solution. In addition, holes are accumulated at the VB of ZnO (+ 3.11 V) in the ZnO<sub>0</sub>/ZnS<sub>60</sub> sample and at the VB of ZnS (+ 2.72 V) in the ZnO<sub>1.5</sub>/ZnS<sub>60</sub> sample due to different carrier transfer mechanisms. Although they can all participate in photocatalytic degradation reactions, the holes in the ZnO<sub>0</sub>/ZnS<sub>60</sub> sample exhibit stronger oxidation ability. Furthermore, it can be seen that for all the samples, the degradation efficiency of MB solution decreases significantly after adding IPA, illustrating that •OH radicals are the main active groups in the photocatalytic reaction of MB solution. In the same way, the contribution of h<sup>+</sup> groups to the degradation of MB solution is determined to be the second, while •O<sub>2</sub> radicals have the least effect.

The EIS properties of the ZnO<sub>0</sub>, ZnO<sub>1.5</sub>, ZnO<sub>0</sub>/ZnS<sub>60</sub> and ZnO<sub>1.5</sub>/ZnS<sub>60</sub> samples are investigated to explore the carrier transfer characteristics of the samples. The EIS Nyquist plot of all the samples shows a standard semicircle, as shown in Fig. 15a.

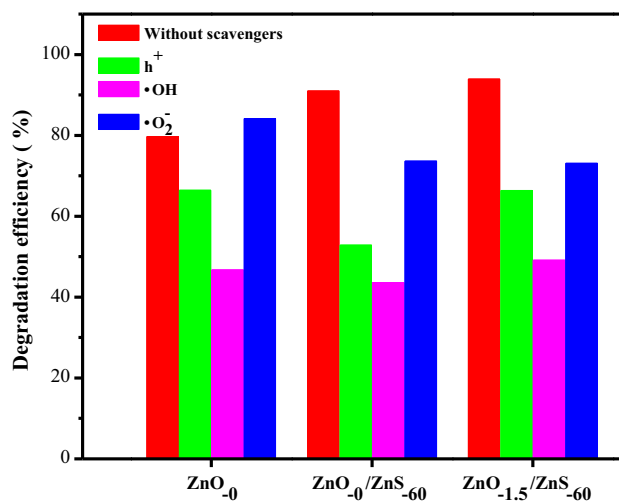


**Figure 14** Active group trapping experiments in the degradation of MB solution photocatalyzed by the ZnO<sub>0</sub>, ZnO<sub>0</sub>/ZnS<sub>60</sub> and ZnO<sub>1.5</sub>/ZnS<sub>60</sub> samples.

The semicircle radius in Nyquist plot illustrates the charge transfer impedance in the sample, and the radius of semicircle indicates the charge transfer impedance of the sample. The smaller the radius, the smaller the impedance. Then, as shown in the figure, the electrochemical impedance of the ZnS sample is the highest, while that of the ZnO<sub>0</sub> sample is the lowest. For the ZnO<sub>1.5</sub> sample, although the free electron concentration increases due to heavy La donor doping, the defect-induced scattering effect results in a decrease in carrier mobility. Therefore, the synergistic effect makes an increase in the sample impedance [34]. After sulfurization, the electrochemical impedance of the ZnO<sub>0</sub>/ZnS<sub>60</sub> and ZnO<sub>1.5</sub>/ZnS<sub>60</sub> samples increases due to the interface barrier between ZnO and ZnS components, but it is still less than that of the ZnS sample, which is consistent with the report [5]. In order to further verify the carrier transfer mechanism difference in the ZnO<sub>0</sub>/ZnS<sub>60</sub> and ZnO<sub>1.5</sub>/ZnS<sub>60</sub> samples, the photocatalytic formation ability of •OH groups by the two samples is investigated with the yield of hydroxyterephthalic acid since terephthalic acid (TA) can react with •OH groups to produce hydroxyterephthalic acid in solution [52, 53]. Due to the consumption of holes by the combination of the CB electrons of ZnO and VB holes of ZnS in Z-scheme carrier transfer mechanism, the formation amount of •OH group in the TA solution photocatalyzed by the composite with Z-scheme carrier transfer mechanism

should be less than that photocatalyzed by the composite with type-II carrier transfer mechanism. As shown in Fig. 15b, the characteristic peak intensity of hydroxyterephthalic acid in solution photocatalyzed by the ZnO<sub>1.5</sub>/ZnS<sub>60</sub> sample is higher than that photocatalyzed by the ZnO<sub>0</sub>/ZnS<sub>60</sub> sample, illustrating that the photo-generated hole amount produced by the ZnO<sub>1.5</sub>/ZnS<sub>60</sub> sample is higher than that by the ZnO<sub>0</sub>/ZnS<sub>60</sub> sample. The results are consistent with the inference that the carrier transfer mechanism in the ZnO<sub>0</sub>/ZnS<sub>60</sub> sample is Z-scheme, while that in the ZnO<sub>1.5</sub>/ZnS<sub>60</sub> sample is type-II.

Based on the above discussions, the photocatalytic mechanism of the ZnO<sub>1.5</sub>/ZnS<sub>60</sub> sample is shown in Fig. 16. According to the type-II carrier transfer mechanism, the photo-generated electrons in the CB of ZnO are transferred to the CB of ZnS, and the photo-generated holes in the VB of ZnS transfer to the VB of ZnO at the same time. Therefore, the photo-generated electrons and holes in the composite are separated into the two different components. The electrons in the CB of ZnO reduce the adsorbed O<sub>2</sub> molecules to •O<sub>2</sub> active groups (O<sub>2</sub>/•O<sub>2</sub> vs. NHE, -0.33 V) and the holes in the VB of ZnS oxidize OH<sup>-</sup> ions in solution to •OH hydroxyl radicals (•OH/OH<sup>-</sup> vs. NHE is +1.99 V and •OH/H<sub>2</sub>O vs. NHE is +2.34 V, respectively) [12]. Both •O<sub>2</sub> active groups and •OH hydroxyl radicals can participate in photocatalytic reaction at the same time, which improves the photocatalytic performance of the composite

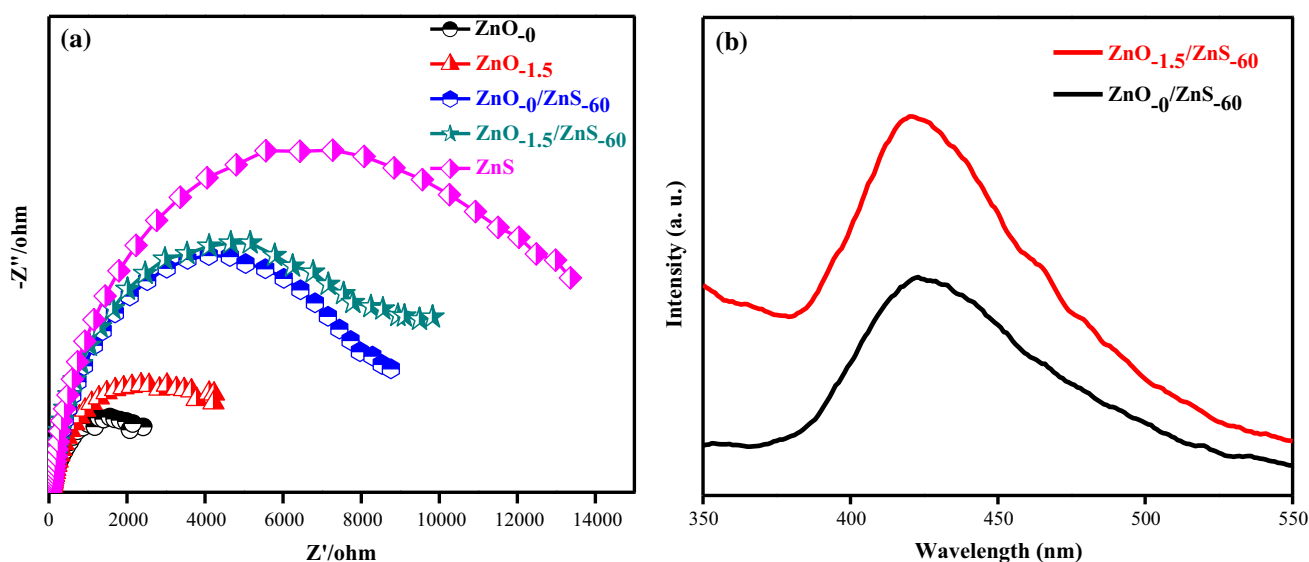


**Figure 15** **a** Nyquist plots of EIS for the ZnO<sub>0</sub>, ZnO<sub>1.5</sub>, ZnO<sub>0</sub>/ZnS<sub>60</sub>, ZnO<sub>1.5</sub>/ZnS<sub>60</sub> and ZnS samples, and **b** Yield of hydroxyterephthalic acid in solution photocatalyzed by the ZnO<sub>0</sub>/ZnS<sub>60</sub> and ZnO<sub>1.5</sub>/ZnS<sub>60</sub> samples, respectively.

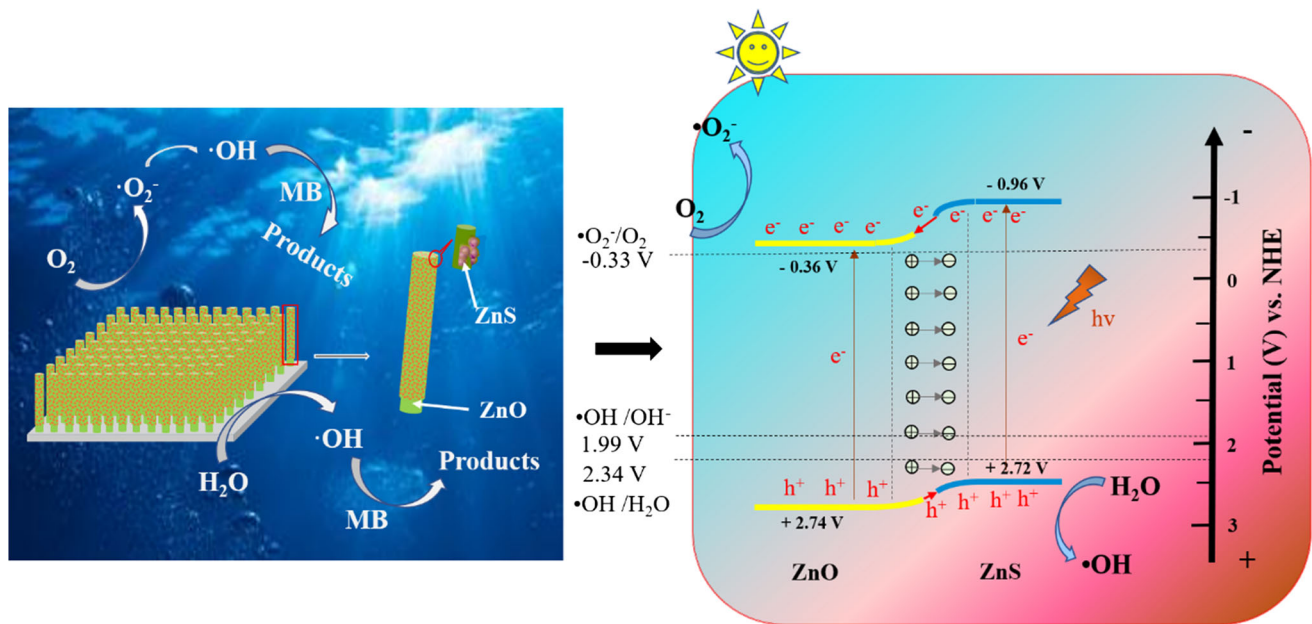


**Figure 16** Schematic diagram of the photocatalytic degradation mechanism of the  $\text{ZnO}_{1.5}/\text{ZnS}_{60}$  composite photocatalyst.

photocatalyst. Figure 11 shows that  $\bullet\text{OH}$  hydroxyl radicals are the main active groups producing catalytic activity. Therefore, the  $\text{ZnO}_{1.5}/\text{ZnS}_{60}$  sample with type-II carrier transfer mechanism shows the best photocatalytic degradation performance.

## Conclusions

$\text{ZnO}$  nanorod-based  $\text{ZnO}_c/\text{ZnS}_T$  series samples were prepared with sol-gel and hydrothermal methods. The effects of La doping concentration in  $\text{ZnO}$  nanorods and sulfurization time on the structural and optical-electric properties of the composite were investigated. Furthermore, the transfer mechanism of photo-generated carriers in composite samples with different La doping concentration was also studied. With the increase in La doping concentration, the  $\text{ZnO}$  (002) peak intensity first increases and then decreases, and the maximum value appears in the  $\text{ZnO}$  nanorods sample with La doping concentration of 1.5%. In addition, with the increase in sulfurization time of  $\text{ZnO}$  nanorods in the composite, the visible light absorption of the composite samples first increases and then decreases, and the maximum value appears in the sample sulfurized for 60 min. In the  $\text{ZnO}_0/\text{ZnS}_{60}$  sample with sulfurization time of 60 min but without La doping, the Fermi level of  $\text{ZnO}$  is less than that of  $\text{ZnS}$ , and the electrons in the

composite are transferred from  $\text{ZnS}$  component to  $\text{ZnO}$  component, thus a built-in electric field is formed in the composite from  $\text{ZnS}$  to  $\text{ZnO}$ . The photo-generated carrier transfer in the  $\text{ZnO}_0/\text{ZnS}_{60}$  composite sample follows a Z-scheme mechanism. While in the  $\text{ZnO}_{1.5}/\text{ZnS}_{60}$  sample with La doping concentration of 1.5% and sulfurization time of 60 min, the heavy La donor doping increases the Fermi level of  $\text{ZnO}$ , and the electrons in the composite are transferred from  $\text{ZnO}$  component to  $\text{ZnS}$  component, thus a new built-in electric field is formed in the composite from  $\text{ZnO}$  to  $\text{ZnS}$ . And its direction is opposite to that of the  $\text{ZnO}_0/\text{ZnS}_{60}$  sample. The photo-generated carrier transfer in the  $\text{ZnO}_{1.5}/\text{ZnS}_{60}$  composite sample follows a type-II mechanism. Therefore, by changing La donor doping concentration in  $\text{ZnO}$  nanorods,  $\text{ZnO}$  nanorods/ $\text{ZnS}$  composite can be prepared with the required carrier transfer mechanism, which provides a basis for the design of  $\text{ZnO}/\text{ZnS}$ -based composites.

## References

- [1] Zhou TS, Wang JC, Chen S, Bai J, Li JH, Zhang Y, Li LS, Xia LG, Rahim M, Xu QJ, Zhou BX (2020) Bird-nest structured  $\text{ZnO}/\text{TiO}_2$  as a direct Z-scheme photoanode with enhanced light harvesting and carriers kinetics for highly efficient and stable photoelectrochemical water splitting.

- Appl Catal B 267:118599. <https://doi.org/10.1016/j.apcatb.2020.118599>
- [2] Li N, Li R, Zhao JH, Liang L, Yu Y, Kong LC, Chen GY, Yan BB (2020) Multi-interface  $\text{Mn}_3\text{O}_4/\text{ZnO}/\text{TiO}_2$  with controllable charge transfer routes for highly selective denitrification under ultrasonic-assisted visible light photocatalysis. *Chem Eng J* 394:124997. <https://doi.org/10.1016/j.cej.2020.124997>
- [3] Witoon T, Numpilai T, Phongamwong T, Donphai W, Boonyuen C, Warakulwit C, Chareonpanich M, Limtrakul J (2018) Enhanced activity, selectivity and stability of a  $\text{CuO-ZnO-ZrO}_2$  catalyst by adding graphene oxide for  $\text{CO}_2$  hydrogenation to methanol. *Chem Eng J* 334:1781–1791. <https://doi.org/10.1016/j.cej.2017.11.117>
- [4] Ahmad W, Basit MA, Khan MS, Ali I, Park TJ (2020) Superior atomic layer deposition of conformal ZnO shell on spherical  $\text{SiO}_2$  particles for enhanced photocatalytic activity. *Physica E Low Dimens Syst Nanostruct* 124:114308. <https://doi.org/10.1016/j.physe.2020.114308>
- [5] Ranjith KS, Castillo RB, Sillanpaa M, Kumar RTR (2018) Effective shell wall thickness of vertically aligned ZnO-ZnS core-shell nanorod arrays on visible photocatalytic and photo sensing properties. *Appl Catal B* 237:128–139. <https://doi.org/10.1016/j.apcatb.2018.03.099>
- [6] Zhang LJ, Li S, Liu BK, Wang DJ, Xie TF (2014) Highly efficient  $\text{CdS}/\text{WO}_3$  photocatalysts: Z-Scheme photocatalytic mechanism for their enhanced photocatalytic  $\text{H}_2$  evolution under visible light. *ACS Catal* 4:3724–3729. <https://doi.org/10.1021/cs500794j>
- [7] Guo ZY, Huo WC, Cao T, Liu XY, Ren S, Yang J, Ding H, Chen K, Dong F, Zhang YX (2020) Heterojunction interface of zinc oxide and zinc sulfide promoting reactive molecules activation and carrier separation toward efficient photocatalysis. *J Colloid Interface Sci* 588:826–837. <https://doi.org/10.1016/j.jcis.2020.11.118>
- [8] Huang ZF, Song JJ, Wang X, Pan L, Li K, Zhang XW, Wang L, Zou JJ (2017) Switching charge transfer of  $\text{C}_3\text{N}_4/\text{W}_{18}\text{O}_{49}$  from II-type to Z-scheme by interfacial band bending for highly efficient photocatalytic hydrogen evolution. *Nano Energy* 40:308–316. <https://doi.org/10.1016/j.nanoen.2017.08.032>
- [9] Zhang Z, John TY (2012) Band bending in semiconductors: chemical and physical consequences at surfaces and interfaces. *Chem Rev* 112(10):5520–5551. <https://doi.org/10.1021/cr3000626>
- [10] Yacobi BG (2004) Semiconductor materials an introduction to basic principles. Kluwer, New York, pp 107–112
- [11] Hui RQ (2020) Introduction to fiber-optic communications. Elsevier, London, pp 79–80
- [12] Kim D, Yong K (2021) Boron doping induced charge transfer switching of a  $\text{C}_3\text{N}_4/\text{ZnO}$  photocatalyst from Z-scheme to II-type to enhance photocatalytic hydrogen production. *Appl Catal B* 282:119538. <https://doi.org/10.1016/j.apcatb.2020.119538>
- [13] Khan TF, Muhyuddin M, Husain SW, Basit MA (2019) Synthesis and characterization of ZnO-ZnS nanoflowers for enhanced photocatalytic performance: ZnS Decorated ZnO nanoflowers. *Int Bhurban Conf Appl Sci Technol (IBCAST)*. <https://doi.org/10.1109/IBCAST.2019.8667220>
- [14] Wang XW, Cao ZQ, Zhang Y, Xu HP, Cao SS, Zhang RB (2020) All-solid-state Z-scheme  $\text{Pt}/\text{ZnS-ZnO}$  heterostructure sheets for photocatalytic simultaneous evolution of  $\text{H}_2$  and  $\text{O}_2$ . *Chem Eng J* 385:123782. <https://doi.org/10.1016/j.cej.2019.123782>
- [15] Luan QR, Chen QF, Zheng J, Guan RF, Fang YF, Hu X (2019) In-situ construction of 2D-ZnS@ZnO Z-scheme heterostructure nanosheet with highly ordered ZnO core and disordered ZnS shell for enhancing the photocatalytic hydrogen evolution. *ChemNanoMat* 6:470–479. <https://doi.org/10.1002/cnma.201900630>
- [16] Pan ZJ, Peng WB, Li FP, Cai YH, He YN (2020) On the piezo-phototronic effect in Si/ZnO heterojunction photodiode: the effect of the fermi-level difference. *Adv Funct Mater* 30(1–11):2005996. <https://doi.org/10.1002/adfm.202005996>
- [17] Adeleye D, Lomuscio A, Sood M, Siebentritt S (2021) Lifetime, quasi-Fermi level splitting and doping concentration of Cu-rich  $\text{CuInS}_2$  absorbers. *Mater Res* 8:025905. <https://doi.org/10.1088/2053-1591/abe3c1>
- [18] Mallick D, Mandal S, Ganesan R, Kumar PSA (2021) Fermi level tuning and the robustness of topological surface states against impurity doping in Sn doped  $\text{Sb}_2\text{Te}_2\text{Se}$ . *Appl Phys Lett* 118:154001. <https://doi.org/10.1063/5.0040697>
- [19] Jia JJ, Takasaki A, Oka N, Shigesato Y (2012) Experimental observation on the Fermi level shift in polycrystalline Al-doped ZnO films. *J Appl Phys* 112:013718. <https://doi.org/10.1063/1.4733969>
- [20] Manik PP, Mishra RK, Kishore VP, Ray P, Nainani A, Huang YC, Abraham MC, Ganguly U, Lodha S (2014) Fermi-level pinning by carrier compensating midgap donor defect band in homoepitaxially grown p-type ZnO by MBE. *Appl Phys Lett* 11:182105. <https://doi.org/10.1063/1.4764909>
- [21] Ye JD, Gu SL, Zhu SM, Liu SM, Zheng YD, Zhang R, Shi Y (2005) Fermi-level band filling and band-gap renormalization in Ga-doped ZnO. *Appl Phys Lett* 86(19):192111. <https://doi.org/10.1063/1.1928322>
- [22] Ryu GH, Bowes PC, McGarrah JR, Irving DL, Dickey EC (2021) Fermi level pinning in Co-doped  $\text{BaTiO}_3$ : Part I. DC



- and AC electrical conductivities and degradation behavior. *J Am Ceram Soc.* <https://doi.org/10.1111/jace.18042>
- [23] Bowes PC, Ryu GH, Baker JN, Dickey EC, Irving DL (2021) Fermi level pinning in Co-doped BaTiO<sub>3</sub>: Part II. Defect chemistry models. *J Am Ceram Soc* 104:5859–5872. <https://doi.org/10.1111/jace.17938>
- [24] Wang ZY, Guo H, Ning D, Ma XB, Zheng LR, Smirnov D, Sun K, Chen DF, Sun LM, Liu XF (2021) Tuning fermi level and band gap in Li<sub>4</sub>Ti<sub>5</sub>O<sub>12</sub> by doping and vacancy for ultrafast Li<sup>+</sup> insertion/extraction. *J Am Ceram Soc* 104:5934–5945. <https://doi.org/10.1111/jace.17948>
- [25] Carroll GM, Schimpf AM, Tsui EY, Gamelin DR (2015) Redox potentials of colloidal n-Type ZnO nanocrystals: effects of confinement, electron density, and fermi-level pinning by aldehyde hydrogenation. *J Am Chem Soc* 137:11163–11169. <https://doi.org/10.1021/jacs.5b06715>
- [26] Huang RM, Ye S, Sun K, Kiang KS, Groot CH (2017) Fermi level tuning of ZnO Films through supercycled atomic layer deposition. *Nanoscale Res Lett* 12:541. <https://doi.org/10.1186/s11671-017-2308-1>
- [27] Wu Y, Guo QX, Zheng Q, Xu XL, Liu T, Liu Y, Yan Y, Wang DW, Long SB, Wang LJ, Yang SW, Teng J, Du SX, Yu GH (2019) Stabilizing the Fermi level of Cr-doped magnetic topological insulators by Al passivation. *J Phys Chem C* 123:3823–3828. <https://doi.org/10.1021/acs.jpcc.8b09661>
- [28] Manik PP, Mishra RK, Kishore VP, Ray P, Nainani A, Huang YC, Abraham MC, Ganguly U, Lodha S (2012) Fermi-level unpinning and low resistivity in contacts to n-type Ge with a thin ZnO interfacial layer. *Appl Phys Lett* 101:182105. <https://doi.org/10.1063/1.4764909>
- [29] Tavkheldize A, Bibilashvili A, Jangidze L, Gorji NE (2021) Fermi-Level Tuning of G-Doped Layers. *Nanomaterials* 11:505. <https://doi.org/10.3390/nano11020505>
- [30] Yu FC, Nan DM, Song TY, Wang BL, Xu BY, He L, Wang S, Duan HY (2020) Photocatalytic degradation characteristics of ZnO/Ag<sub>2</sub>CrO<sub>4</sub> composite and its Z-type electron transport photocatalytic mechanism. *Materials Reports* 34(4):08003–08009. <https://doi.org/10.11896/cldb.19050190>
- [31] Yu FC, Song TY, Wang BL, Xu BY, Li HS, Hu HL, He L, Duan HY, Wang S, Tang XX (2019) The effects of intrinsic defects on the structural and optical properties of ZnO thin film prepared via a sol-gel method. *Mater Res Express* 6(11):115901. <https://doi.org/10.1088/2053-1591/ab4394>
- [32] Li Q, Hu J, Zhou Y, Wang HQ, Wu ZB (2021) La-Doped BiOI microspheres for efficient photocatalytic oxidation of NO under visible light illumination. *Acta Phys-Chim Sin.* 37 (8): 2009100 (1–10). doi: <https://doi.org/10.3866/PKU.WHXB202009100>
- [33] Bomila R, Srinivasan S, Gunasekaran S, Manikandan A (2018) Enhanced photocatalytic degradation of methylene blue dye, opto-magnetic and antibacterial behaviour of pure and La-doped ZnO Nanoparticles. *J Supercond Nov Magn* 31:855–864. <https://doi.org/10.1007/s10948-017-4261-8>
- [34] Zhou J, Zhao J, Liu R (2020) Defect engineering of zeolite imidazole framework derived ZnS nanosheets towards enhanced visible light driven photocatalytic hydrogen production. *Appl Catal B* 278:119265. <https://doi.org/10.1016/j.apcatb.2020.119265>
- [35] Patil RP, Mahadik MA, Bae HS, Chae WS, Choi SH, Jang JS (2020) Porous Zn<sub>1-x</sub>Cd<sub>x</sub>S nanosheets/ZnO nanorod heterojunction photoanode via self-templated and cadmium ions exchanged conversion of ZnS(HDA)<sub>0.5</sub> nanosheets/ZnO nanorod. *Chem. Eng. J.* 402: 126153. <https://doi.org/10.1016/j.cej.2020.126153>
- [36] Kim MW, Joshi B, Samuel E, Seok H, Aldalbahi A, Almoqli M, Swihart MT, Yoon SS (2020) Electrospayed MnO<sub>2</sub> on ZnO nanorods with atomic layer deposited TiO<sub>2</sub> layer for photoelectrocatalytic water splitting. *Appl Catal B* 271:118928. <https://doi.org/10.1016/j.apcatb.2020.118928>
- [37] Wang S, Zhu BC, Liu MJ, Zhang LY, Yu JG, Zhou MH (2019) Direct Z-scheme ZnO/CdS hierarchical photocatalyst for enhanced photocatalytic H<sub>2</sub>-production activity. *Appl Catal B* 243:19–26. <https://doi.org/10.1016/j.apcatb.2018.10.019>
- [38] Long XF, Gao LL, Li F, Hu YP, Wei SQ, Wang CL, Wang T, Ma JJ (2019) Bamboo shoots shaped FeVO<sub>4</sub> passivated ZnO nanorods photoanode for improved charge separation/transfer process towards efficient solar water splitting. *Appl Catal B* 257:117813. <https://doi.org/10.1016/j.apcatb.2019.117813>
- [39] Gao F, Yuan J, Huang XY, Lei R, Jiang C, Zhuang JD, Liu P (2021) Directional transfer of photo-generated charges mediated by cascaded dual defects in ternary photocatalyst ZnS/ZnO-In<sub>2</sub>O<sub>3</sub> with enhanced photocatalytic performance. *Chem Eng J* 416:129159. <https://doi.org/10.1016/j.cej.2021.129159>
- [40] Wang AQ, Zhang L, Rahimi MG, Gong SY, Nie LF, Han N, Chen YF (2020) Defect engineering of ZnO for electron transfer in O<sub>3</sub> catalytic decomposition. *Appl Catal B* 277:119223. <https://doi.org/10.1016/j.apcatb.2020.119223>
- [41] Qu YN, Xu XJ, Huang RL, Qi W, Su RX, He ZM (2020) Enhanced photocatalytic degradation of antibiotics in water over functionalized N, S-doped carbon quantum dots embedded ZnO nanoflowers under sunlight irradiation. *Chem Eng J* 382:123016. <https://doi.org/10.1016/j.cej.2019.123016>
- [42] Li JPH, Zhou XH, Pang YQ, Zhu L, Vovk EI, Cong L, Bavel AP, Li SG, Yang Y (2019) Understanding of binding energy calibration in XPS of lanthanum oxide by in situ treatment.

- Phys Chem Chem Phys 21(40):22351–22358. <https://doi.org/10.1039/c9cp04187g>
- [43] Li SY, Huang XF, Wan ZY, Liu J, Lu LJ, Peng KM, Schmidt-Ott A, Schmidt-Ott RB, Bhattarai R (2020) Green synthesis of ultrapure La(OH)<sub>3</sub> nanoparticles by one-step method through spark ablation and electrospinning and its application to phosphate removal. *Chem Eng J* 388:124373. <https://doi.org/10.1016/j.cej.2020.124373>
- [44] Zhang K, Dong TJ, Xie GC, Guan LM, Guo BD, Xiang Q, Dai YW, Tian LQ, Batool A, Jan SU, Boddula R, Thebo AA, Gong JR (2017) Sacrificial interlayer for promoting charge transport in hematite photoanode. *ACS Appl Mater Interfaces* 9(49):42723–42733. <https://doi.org/10.1021/acsami.7b13163>
- [45] Guo BD, Tian LQ, Xie WJ, Batool A, Xie GC, Xiang Q, Jan SU, Boddula R, Gong JR (2018) Vertically aligned porous organic semiconductor nanorod array photoanodes for efficient charge utilization. *Nano Lett* 18(9):5954–5960. <https://doi.org/10.1021/acs.nanolett.8b02740>
- [46] Li CC, Li A, Luo ZB, Zhang JJ, Chang XX, Huang ZQ, Wang T, Gong JL (2017) Surviving high-temperature calcination: ZrO<sub>2</sub>-induced hematite nanotubes for photoelectrochemical water oxidation. *Angew Chem Int Ed* 56(15):4150–4155. <https://doi.org/10.1002/anie.201611330>
- [47] Ahsaine HA, Slassi A, Naciri Y, Chennah A, Jaramillo-Pa'ez C, Anfar Z, Zbair M, Benlhachemi A, Navi'ó J A, (2018) Photo/Electrocatalytic properties of nanocrystalline ZnO and La-Doped ZnO: combined DFT fundamental semiconducting properties and experimental study. *ChemistrySelect* 3:7778–7791. <https://doi.org/10.1002/slct.201801729>
- [48] Ali G, Zaidi SJA, Basit MA, Park TJ (2021) Synergetic performance of systematically designed g-C<sub>3</sub>N<sub>4</sub>/rGO/SnO<sub>2</sub> nanocomposite for photodegradation of Rhodamine-B dye. *Appl Surf Sci* 570:151140. <https://doi.org/10.1016/j.apsusc.2021.151140>
- [49] Chen YJ, Zhu PF, Duan M, Li J, Ren ZH, Wang PP (2019) Fabrication of a magnetically separable and dual Z-scheme PANI/Ag<sub>3</sub>PO<sub>4</sub>/NiFe<sub>2</sub>O<sub>4</sub> composite with enhanced visible-light photocatalytic activity for organic pollutant elimination. *Appl Surf Sci* 486:198–211. <https://doi.org/10.1016/j.apsusc.2019.04.232>
- [50] Wang YC, Zhanga A, Zhang D, Zhoua PY, Wanga RR, Xiang J, Zhang XM, Su S (2019) Ag<sub>2</sub>CO<sub>3</sub> anchored on BiOI/CoFe<sub>2</sub>O<sub>4</sub> composites with p-n-p heterojunctions: highly enhanced activity for photocatalytic oxidation of Hg-0 under fluorescent light irradiation. *Colloid Surf A-Physicochem Eng* 579:123654. <https://doi.org/10.1016/j.colsurfa.2019.123654>
- [51] Sin JC, Lam SM, Zeng HH, Lin H, Li HX, Kumaresan AK, Mohamed AR, Lim JW (2020) Z-scheme heterojunction nanocomposite fabricated by decorating magnetic MnFe<sub>2</sub>O<sub>4</sub> nanoparticles on BiOBr nanosheets for enhanced visible light photocatalytic degradation of 2,4-dichlorophenoxyacetic acid and Rhodamine B. *Sep Purif Technol* 250:117186. <https://doi.org/10.1016/j.seppur.2020.117186>
- [52] Ma DD, Shi JW, Sun DK, Zou YJ, Cheng LH, He C, Wang HK, Niu CM, Wang LZ (2019) Au decorated hollow ZnO@ZnS heterostructure for enhanced photocatalytic hydrogen evolution: The insight into the roles of hollow channel and Au nanoparticles. *Appl Catal B* 244:748–757. <https://doi.org/10.1016/j.apcatb.2018.12.016>
- [53] Zhang F, Li YH, Qi MY, Tang ZR, Xu YJ (2020) Boosting the activity and stability of Ag-Cu<sub>2</sub>O/ZnO nanorods for photocatalytic CO<sub>2</sub> reduction. *Appl Catal B* 268:118380. <https://doi.org/10.1016/j.apcatb.2019.118380>

**Publisher's Note** Springer Nature remains neutral with regard to jurisdictional claims in published maps and institutional affiliations.